



Binnie, S.A. et al. (2020) The origins and implications of paleochannels in hyperarid, tectonically active regions: the northern Atacama Desert, Chile. *Global and Planetary Change*, 185, 103083. (doi: [10.1016/j.gloplacha.2019.103083](https://doi.org/10.1016/j.gloplacha.2019.103083))

There may be differences between this version and the published version. You are advised to consult the publisher's version if you wish to cite from it.

<http://eprints.gla.ac.uk/203619/>

Deposited on 19 November 2019

Enlighten – Research publications by members of the University of Glasgow
<http://eprints.gla.ac.uk>

The origins and implications of paleochannels in hyperarid, tectonically active regions: The northern Atacama Desert, Chile

S. A. Binnie^{a,1}; K. R. Reicherter^b; P. Victor^c; G. Gonzalez^{d,e}; A. Binnie^a; K. Niemann^b; F.M. Stuart^g; C. Lenting^a; S. Heinze^f; S.P.H.T. Freeman^g; T. J. Dunai^a

^a Institute of Geology and Mineralogy, University of Cologne, 50674 Cologne, Germany

^b Neotectonics and Natural Hazards, RWTH Aachen University, 52056 Aachen, Germany

^c Helmholtz-Zentrum Potsdam Deutsches GeoForschungsZentrum (GFZ) 14473 Potsdam, Germany

^d Departamento de Ciencias Geológicas Universidad Católica Del Norte, Antofagasta, Chile

^e National Research Center for Integrated Natural Disaster Management (CIGIDEN), Vicuña Mackenna, 4860, Santiago, Chile

^f Institut für Kernphysik, University of Cologne, 50937 Cologne, Germany

^g Scottish Universities Environmental Research Centre (SUERC), East Kilbride G75 0QF, UK

¹ corresponding author

Keywords: paleodrainage; channel abandonment; multiple cosmogenic nuclides; hyperaridity; uplift rates; Pampa de Tana

Abstract

Preserved remnants of fluvial activity in deserts constitute evidence for changing boundary conditions. The Atacama Desert of northern Chile is the global end-member for aridity, so the history of relict stream networks in this region is a record of how landscapes develop under extreme conditions. On Pampa de Tana in northern Chile (19.4°S), a series of channel forms that are presently inactive but in the past flowed westward are incised into the surface of a fault bounded, topographically elevated portion of the El Diablo Formation, a regionally extensive, relict pediment. We measure cosmic-ray produced ^{10}Be , ^{26}Al and ^{21}Ne in fluvial deposits to date the timing of abandonment of three channels and couple this with topographic profile information from a SPOT-6 derived, 2 m resolution digital elevation model. We find two of the channels were abandoned approximately >5.6 Myr and 2.0 Myr ago. One channel is still capable of flow and has ages suggesting it was fluvially active within the last few hundred thousand years. Using the paleochannel ages measured here and published ages for the end of aggradation of the El Diablo Formation we estimate the rates of fluvial channel incision before channel abandonment, and uplift rates on the faults after channel abandonment. Maximum uplift rates of ~12 m/Myr over the last 2 Myr are found. In general, while rates of uplift are relatively low they are several-fold more rapid than the rates of fluvial incision prior to channel abandonment. This implies that westward channel flow was interrupted by uplift of topography above a blind NW-SE striking reverse fault that affects the Central Depression, an alluvial forearc basin. We consider also that shrinkage of the upstream catchment area by stream capture, promoted via headward erosion and lateral expansion of adjacent canyons (quebradas) could be a factor in the abandonment of the channels on Pampa de Tana. Our results highlight the polygenetic nature of this landscape and show that relatively minor amounts of fault displacement in hyperarid regions can have implications for stream network evolution. Even subtle topographic uplift upstream should be taken into account when fluvial deposits are used as proxies for long-term environmental conditions.

1. Paleochannels of the northern Atacama Desert

Stream channels are sensitive indicators of change in the majority of landscapes, able to adapt rapidly to varying environmental conditions. Understanding adjustments of stream courses can provide insights into both past climatic conditions and relief forming tectonic processes (e.g. Amos et al. 2010; García and Hérail., 2005; Hampel and Hetzel, 2016; Humphrey and Konrad, 2000; Jackson et al 1996; Jansen et al., 2013; Keller et al., 1998; Ouchi, 1985). Small, unconfined, desert streams are particularly useful in this respect as they are often close to thresholds for change and can be influenced by relatively subtle variations in their controlling tectonic and climatic factors (Pearce et al., 2004; Schumm et al., 2000; Tooth, 2013). At the same time, care must be taken when untangling the effects of climate and tectonics alongside adaptations that can occur in dryland fluvial systems without any changes in external influences (Vandenberghe, 2003). Robust chronologies of drainage adaptation are key to their usefulness as a proxy for revealing and isolating forcing mechanisms of landscape evolution but such chronologies are often unavailable (Reid, 2009; Tooth, 2012).

The prevalence of ancient but well preserved, abandoned stream channels in the northern Chilean Atacama Desert attests to the long-term hyperaridity of this region (Carrizo et al., 2008; García and Hérail., 2005; Ritter et al., 2018a). However, this notion of environmental stability is juxtaposed with the nature of the landforms themselves, in that there must be some causal mechanism to explain their abandonment. Channels traversing tectonically active, uplifting topography are often termed transverse drainages, or watergaps. Following defeat and rerouting of a stream, the remaining elevated 'dry' valley may be labelled a windgap; though the term windgap is often applied more broadly to any raised notch on a ridge, so here we refer more specifically to paleochannels that retain some qualitative characteristics of streams. The response of streams that traverse a growing fold have been discussed by Humphrey and Konrad (2000), who suggest that the concept of stream power used to model bedrock erosion is a poor predictor of how channels will adapt to uplift. They propose that it is not the ability of

the stream to incise into the uplifting topography that will dictate whether or not it is defeated, instead defeat will depend on whether or not alluvial deposition upstream of the growing fold manages to raise the channel bed concomitantly with the uplift of the antecedent channel. A watergap will be maintained until the rate of uplift exceeds the rate of sediment deposition, whereby the stream becomes blocked and a paleochannel or windgap may be preserved. However, other studies have found the lithology of the rising topography is a control (Collignon et al., 2016), suggesting the incision capability and thus in some sense the stream power of transverse drainage is important. Whether it is the transport and deposition of alluvial material upstream of the uplifting topography raising the channel bed, or the streams ability to incise the growing fold that is the key in deciding if stream channels can keep pace with uplift, both scenarios require sufficient discharge. Some modelling studies show aridification controls windgap formation, supporting a climatic driver for channel abandonment (Hampel and Hetzel, 2016), while others find a combination of rapid uplift and low precipitation are needed to defeat drainage traversing uplifting faults (e.g. Sobel et al., 2003). Modelling by Tomkin and Braun (1999) predicts windgaps can form under constant uplift with no change in climatic conditions, challenging the notion of Jackson et al. (1996), that windgaps found in a New Zealand study were controlled by a combination of the periodicity of earthquake and climate cycles.

In this paper we establish a chronology for stream channel abandonment at a site on the Pampa de Tana (~19.4°S), in the Tarapacá region of the northern Atacama Desert. The antiquity of preserved fluvial features in the Atacama Desert can make estimating their age challenging, often requiring dating to extend into the Miocene (Dunai et al., 2005; Nishiizumi et al., 2005). We date the timing of abandonment by measuring cosmic-ray produced ^{10}Be , ^{26}Al and ^{21}Ne exposure ages of fluvial channel deposits and compare this chronology with detailed channel and topographic profiles derived from SPOT-6 satellite imagery. Differing age interpretations between the different isotopes and saturated radionuclide concentrations are addressed. We discuss the implications of our study for the ongoing

debate regarding the climatic history of the region. Rates of fluvial incision are estimated and related to rates of underlying fault displacement and we appraise the likely causes of channel abandonment. Lastly, we consider our findings in light of the broader-scale tectonic history of the region and reflect on how constraining drainage reorganization in the vein of what we find here might be combined with studies of biological evolution and extraterrestrial geomorphology.

2. Field area

2.1 Regional setting

The Atacama Desert contains the ‘oldest’ remnant landscapes in the world (Dunai et al., 2005; Nishiizumi et al., 2005; Kober et al., 2007). The pervading landscape stability of the region is linked to its extreme hyperaridity, but when that period of stability began and how consistent it has been is contentious, with proponents arguing for the onset of hyperarid conditions as recently as the Pleistocene and as long ago as the Miocene/Oligocene (Alpers and Brimhall, 1988; Amundson et al., 2012; Dunai et al., 2005; Evenstar et al., 2009; Hartley, 2003; Hartley and Chong, 2002; Jordan et al., 2014; Nishiizumi et al., 2005). Several authors have also pointed to evidence that there have been episodic wetter, though still arid, periods within these time-frames, questioning the notion that the landscape is entirely stable over several millions of years (Dunai et al., 2005; Evenstar et al., 2009; Garcia et al. 2011; Houston and Hartley, 2003; Oerter et al., 2016; Placzek et al., 2010; Ritter et al., 2019; Sáez et al., 2012), while others note the spatial context and type of proxy used in individual studies may help resolve discrepancies between the various studies (Jordan et al., 2014; Ritter et al., 2018a).

With aridity retarding denudation, the gross topographic form of northern Chile has been dictated by large-scale tectonic structures. The Central Depression (Pampa del Tamarugal) is a north-south elongated forearc sedimentary basin situated between the Western Precordillera of the Andes to the

east and the Coastal Cordillera to the west (Figure 1A). The topography of the Western Precordillera rises from approximately 1 km average elevation in the Central Depression to higher than 4 km towards the Altiplano and its overall smooth form has led to it being described as a crustal scale monocline (Isacks, 1988), elevated by uplift on several west vergent thrust faults in the Precordillera (Farías et al, 2005; García and Hérail, 2005; Muñoz and Charrier, 1996; Victor et al., 2004). The timing of this uplift is still debated but is generally agreed to have occurred during the Cenozoic (Farías et al., 2005; Garcia et al., 2011).

<<Approximate location of figure 1 >>

The macroscale drainage pattern of northern Chile between approximately 18.5°S and 19.5° S is one where catchments source most of their stream discharge in the High Andes or Precordillera (Mortimer, 1980) and flow westwards, through the hyperarid basin of the Central Depression on their path to the Pacific Ocean (Figure 1A), in some cases breaching the northern tip of the Coastal Cordillera before this mountain range ends at the city of Arica. Further south of around 19.5°S, the catchments emanating from the Precordillera are endorheic, draining internally into the Central Depression. The major channels, or quebradas, traversing the Central Depression typically take one of two forms; either deeply incised canyons, the channels and steep side slopes of which contrast with the surrounding low relief pediplain, or broad braided channels that may not have incised notably into the pediplain surface at all (Mortimer and Sarič, 1972; Mortimer, 1980).

The basin of the Central Depression contains a succession of fluvio-lacustrine and alluvial gravel deposits. The upper surface of these gravels onlaps the western flanks of the Andean Precordillera as a series of coalesced pediments and abandoned fan surfaces, resulting in an elongated, approximately

north-south oriented pediplain between around 18°S to 22°S, termed the Tarapaca Pediplain by Mortimer and Saric (1975). These deposits, or their eroded surfaces, have been used in arguments for the long-term climatic conditions that would have prevailed during their formation over the last circa 19 Myr, or more (Evenstar et al., 2017, and references therein). The El Diablo Formation mantles the Pampa de Tana and surrounding areas with coalesced alluvial and fluvial fan matrix supported gravel deposits (García et al., 2013; Figure 2A), considered to derive predominantly from erosion of andesitic lava of the Eastern Precordillera and Western Cordillera (Charrier et al., 2013; Farías et al., 2005; García and Hérail, 2005; Pinto, 2004). Dating of overlying and interfingering lavas and interbedded tuffs, plus stable cosmogenic isotope surface exposure dating have placed temporal constraints on when deposition of the El Diablo Formation ceased. Farías et al. (2005) ascribe an upper and a lower unit to the El Diablo Formation and propose an 11.7 ± 0.4 Myr age for deposition at the base of the upper unit from a single K/Ar age. Based mostly on the K-Ar and Ar-Ar ages of Blanco and Tomlinson (2013) and Jordan et al (2010), who dated interbedded volcanic material, Jordan et al. (2014) propose that deposition of the El Diablo Formation gravels had ended by 11-12 Myr. Evenstar et al. (2017), using cosmogenic nuclide exposure dates of surface clasts suggest a regional hiatus in deposition 11 Myr ago. An earlier span of between 11 and 7.5 Myr for the deposition of the El Diablo Formation from exposures in the valley of Quebrada de Camarones has been proposed by von Rotz et al. (2005), using an interbedded 8.2 Myr old tuff and magnetostratigraphy. However, García et al. (2011) suggest this age range is too young, as it is inconsistent with the generally accepted 8.3 ± 0.5 Myr age for the Tana lava that overlies the El Diablo Formation (García et al., 2004; Mortimer et al., 1974; Naranjo and Paskoff, 1985; Muñoz and Sepúlveda, 1992).

2.2 Local setting of the Pampa de Tana paleochannels

The triangular shaped surface comprising the Pampa de Tana lies between the Quebrada de Camarones and Quebrada de Camiña and slopes on average 4° to the south-west (Figure 1B, Figure 2B). The eastern portions act as the modern catchment heads for the surface drainages that are flowing westwards. Presumably, prior to the incision or lateral expansion of the bounding Quebradas, the streams flowing over the Pampa de Tana had their headwaters at higher elevations to the east. This notion is supported by the remnant thin tongue of Tana lava that is found overlying the El Diablo Formation at the north eastern edge of the pampa (García et al., 2011; 2013), and which would have flowed downhill (to the west) from higher elevations (see also section 2.1). A once more expansive eastern Pampa de Tana is also evident in the beheaded streams that can be found around the eastern edge of the pampa and this will be discussed in more detail in section 6.2. Presently, the eastern apex of the wedge-shaped surface that is Pampa de Tana tapers to a narrow ridge that acts as a drainage-divide between the bounding Quebrada de Camarones and Quebrada de Camiña (Figure 1B).

<<Approximate location of figure 2 >>

The low relief, planar form of the Pampa de Tana surface is interrupted by an east facing and northwest-southeast oriented scarp (herein termed the eastern scarp), as much as forty meters high, which marks the eastern extent of an elongated topographic bulge (Figure 2, B-B', Figure 3A). A few kilometers to the west, the extents of this bulge are delineated by a less well defined, south-westward facing scarp. The approximate locations of the eastern and western scarps, and other scarps in the area, are suggested by Garcia et al. (2013) to be monoclonal flexures, based on 1:100 000 scale mapping (Figure 3C).

Several sinuous channel forms with widths of a few meters to a few tens of meters have been incised 20 m or more into the smooth crest of the topographic bulge (Figures 3A, Figures 4A and 4B). That these features contain channel bars of coarser, rounded cobble material attests to their fluvial nature (Figure 4A). Evenstar et al. (2017) report several cosmogenic ^3He derived exposure ages from the Pampa de Tana area. They targeted the pediment surfaces in order to constrain the timing of deposition, or aggradation, of these fluvial-lacustrine gravels and mapped a contact between two different generations of pediment surface along the eastern scarp. The ages that Evenstar et al. (2017) derive from six samples split between two proximal sites upstream of the topographic bulge range between approximately 1 to 7 Myr. The same authors measured ^3He in three samples collected from the crest of the bulge (Figure 3D) and obtain ages of between around 11 to 20 Myr.

<<Approximate location of figure 3 >>

3. Methods

3.1. Sample preparation and measurement

3.1.1. ^{10}Be and ^{26}Al

Pebble and cobble samples were collected from three paleochannel sites and two sites on the crest of the topographic bulge (Figure 3D, Figure 4). Samples were mostly pure quartz and ranged in size from around 1 – 10 cm in diameter, often with a dark desert varnish patina. One fluvial sediment sample was collected from the Quebrada de Camiña, a few km downstream of the paleochannel sampling locations. From each site sampled, several single clast samples were chosen based on quartz content, size and evidence for fluvial rounding. The samples were documented, crushed and sieved to retain the 250 –

710 μm size fraction. During crushing the samples often exhibited conchoidal fracturing, typical of microcrystalline varieties of quartz. The sample of fluvial sediment from the active Quebrada de Tiliviche was sieved in the field to retain the 250 – 710 μm fraction. Initially, seven samples were prepared as AMS (Accelerator Mass Spectrometry) targets for $^{10}\text{Be}/^9\text{Be}$ at the University of Edinburgh using the chemistry protocols described in Binnie et al. (2007). These targets were measured at SUERC (Scottish Universities Environmental Research Centre) AMS (Xu et al., 2010) normalized to the NIST SRM 4325 standard with an assumed nominal value of 3.06×10^{-11} . Later, twenty-one further samples were prepared as ^{10}Be targets at the University of Cologne using the quartz etching scheme of Kohl and Nishiizumi (1992) and the stacked column approach described in Binnie et al. (2015). These targets were measured at CologneAMS (Dewald et al., 2013) normalized to the standards of Nishiizumi et al., (2007). $^{26}\text{Al}/^{27}\text{Al}$ measurements were made at CologneAMS on nine out of the twenty-one samples prepared at the University of Cologne, with AMS measurements normalized to the standards reported by Nishiizumi et al. (2004) (see supplementary data). ^{27}Al determinations on aliquots taken after quartz dissolution were measured using in-house ICP-OES (inductively coupled plasma – optical emission spectrometry) using standard addition (4 aliquots). For quality control, measurements of NIST SRM-165a were included alongside the samples during ICP-OES analysis.

<<Approximate location of figure 4 >>

Concentrations of ^{10}Be and ^{26}Al were derived following the subtraction of any atoms measured in reagent blanks that were prepared in tandem with the samples, as described in Binnie et al. (2019). The one standard deviation analytical uncertainties in our ^{10}Be concentrations include the propagated measurement uncertainty on the AMS ratios of both the samples and the associated blank, and a 1%

estimate for the one standard deviation uncertainty in the masses of ^9Be added as carrier. Uncertainties in the ^{26}Al concentrations come from the propagation of the uncertainties derived from the ICP-OES ^{27}Al measurements, which are between 3.5% and 4.9%, with the uncertainties in the AMS ratios. Exposure ages were derived using version 3 (wrapper 3.0.2, constants 3.0.4) of the online calculator formerly known as the Cronus calculator (Balco et al., 2008).

To investigate the possibility that our samples were buried during their exposure history we plot ^{10}Be concentrations against respective ratios of $^{26}\text{Al}/^{10}\text{Be}$, for the samples where ^{26}Al measurements were made. For these plots, termed two-isotope diagrams, the envelope, or 'island', of constant exposure requires production rates scaled to the sample site. We use the elevation and coordinates of site 5 but note that using one of the other sample sites makes negligible difference to the position of the constant exposure island. Two different time-dependent spallogenic production rate scaling schemes were considered when constructing the two-isotope diagrams. Spallogenic production rate scaling factors for ^{10}Be and ^{26}Al are derived over the last 10 Myr following Lifton et al. (2014) and the average scaling factors over this period, weighted by the respective rates of decay of ^{10}Be (1.39 Myr) and ^{26}Al (705 kyr), are multiplied by the production rates of 3.92 at/g/a and 28.54 at/g/a. These are the equivalent sea-level, high-latitude values reported by Borchers et al. (2016) to give the best fits to the global calibration site datasets (termed 'Sa' in Borchers et al., 2016). We refer to this approach below as the LSD scaling scheme. Spallogenic production was also determined using the Lm scaling scheme described in Balco et al. (2008), with the time-varying values for cut-off rigidity (R_c) derived according to Lifton et al. (2014), weighted by respective rates of decay over 10 Myr. The resulting scaling factors are multiplied by the respective best fit production rates of 4.00 at/g/yr and 27.93 at/g/yr (termed 'Lm' in Borchers et al., 2016). Muogenic production, which will be only a small fraction of the total production, is scaled using the simplified approach detailed in Balco et al. (2017). We use the resulting site specific spallogenic and muogenic ^{10}Be and ^{26}Al production rates to plot the two-isotope diagrams.

3.1.2. ^{21}Ne

Quartz from the 250–710 μm fraction of the acid etched mineral separates prepared for ^{10}Be and ^{26}Al was packed into aluminum foil containers for ^{21}Ne determinations. Neon was extracted by heating in a double-walled ultra-high vacuum furnace at 1200°C and the isotope composition determined using a Mass Analyser Products 215-50 mass spectrometer at SUERC in 2014 and in 2016 (Codilean et al. 2008). CREU quartz standards were measured at the same time (Vermeesch et al., 2015). In several cases samples were measured in duplicate or triplicate. Age determinations were made using version 3 (wrapper 3.0.2, constants 3.0.4) of the online calculator formerly known as the CRONUS calculator (Balco et al., 2008). This assumes that the samples contain a mixture of air- and spallation-derived Ne. Where replicate measurements have been made we have determined a mean exposure age.

3.1.3. Raman Spectrometry

Six of the twelve samples with both ^{10}Be and ^{21}Ne determined were subjected to Raman spectrometry (Table 2). The Raman spectra were obtained from randomly selected grains of the crushed and sieved <250 μm fraction with a Renishaw InVia Raman microscope at the University Cologne. The spectra were produced after manually focusing the laser with a x10 objective (NA = 0.25) immediately below the grain surface for 100 x 1 sec with a 532 nm Ne:YAG laser combined with a 3200 lines/mm grating and a Centrus 05TJ CCD detector. Spectrometer calibration was performed before and between analyses with a built-in silicon standard.

3.2. Topographic surface models and profiles

Epipolar images and subsequently a 2 m DEM (digital elevation model) were derived from a SPOT-6 stereopair of 1.5 m resolution using Geomatica 2018 software (Figure 3B). Ground control points identifiable in both images were mostly manmade features and river channel junctions. Artifacts, noise, and to a certain extent the visible manmade features of the surface mine were smoothed using the proprietary filters in the DSM2DTM module. The ArcGIS v.10 AddIn tool, described by (Pérez-Peña et al., 2017), is used to generate swath profiles along the channels from which samples were collected for cosmogenic nuclide analysis (Figure 3D). This tool can plot maximum and minimum topographic elevations in a swath of specified width along a multi-directional user defined path. In this case, our 500 m wide swaths follow the course of the channels incised into the topographic bulge, allowing us to generate elevation profiles along the channel bed, or thalweg (the lowest elevations along the swath) and profiles of the channel-banks (the highest elevations along the swath). We used the same tool to derive a 500m wide topographic swath showing relief along the eastern scarp (Figure 3D).

4. Results

4.1. Sample lithology

Besides the main quartz band at around 465 cm^{-1} , all Raman spectra reveal peaks of varying intensity at 503 cm^{-1} (Figure 5). This can be assigned to moganite (e.g. Heaney and Post, 1992), which, when intergrown with quartz is indicative of chalcedony. Schmidt et al. (2012) recently reported that molecular vibrations of “free Si-O” bonds of silanol (Si-OH) groups (503 cm^{-1}) on the quartz grain surface may overlap with the moganite band. Thus it is unclear whether the samples consist of fine quartz-moganite intergrowths, or microcrystalline quartz with a high surface area and consequently a greater capacity for silanol groups. Regardless of this, these samples are not monocrystalline quartz. While

most of these samples appear to consist of pure SiO₂ polymorphs, sample TA06-IG contains small amounts of anatase (TiO₂). Additionally, this sample reveals rough surfaces and appears less translucent than other samples.

<<Approximate location of figure 5 >>

4.2. Cosmogenic radionuclide concentrations and exposure age interpretation

Concentrations of ¹⁰Be, ²⁶Al and ²¹Ne are reported in Table 1, following blank subtraction. All ¹⁰Be blank subtractions were 1.0% or less of the total number of atoms measured in the samples, except TA1A, TA3B and PIS15-5, which required subtractions of 2.6%, 10.0% and 5.6% of the total ¹⁰Be measured in the respective targets. The largest blank subtraction for ²⁶Al was 0.6%, except for sample PIS12-5, where it was 4.9% of the total number of ²⁶Al atoms measured in the sample. The ages derived from the concentrations are shown in Table 2.

<<Approximate location of table 1 >>

<<Approximate location of table 2>>

After a period of time equivalent to four half-lives, ¹⁰Be and ²⁶Al concentrations in non-eroding samples will have reached 94% of their saturated concentrations. We thus assume the reliable upper limit of our ¹⁰Be and ²⁶Al exposure ages to be 5.6 Myr and 2.8 Myr respectively, or four times the half-lives of ¹⁰Be and ²⁶Al. In some cases, the online calculator of Balco et al. (2008) reported ages older than this and we

have supposed those samples to be close enough to saturation to be reported as such. In any case, we note the uncertainty on these 'close to saturation' ages was >40%.

The ^{10}Be exposure age results based on the LSD scaling scheme and zero erosion show saturation of all the samples located on the interfluves and all the samples collected from the northernmost channels (Figure 6) (Table 2). As discussed above, we propose all these samples are older than 5.6 Myr. One ^{26}Al interfluve result gives an age that is slightly less than saturation and this might indicate recent, relatively shallow burial, but in general the saturation of the interfluve samples suggests long-term surface stability of the interfluves. In the central channel the ages range from saturation to 2.0 Myr, while at the southern channel the ages range from 1.5 Myr to 0.1 Myr (Figure 6). In general, exposure ages within the channels decrease towards the south. The interfluves are older than the central and southern channels but it is not possible to determine by how much the northern channel is younger than the interfluves.

<<Approximate location of figure 6 >>

We plot the ^{10}Be and ^{26}Al results on the two-isotope diagrams shown in Figures 7A and 7B. The difference between 7A and 7B is the scaling scheme used (LSD and Lm respectively). It is clear from these plots that several of the interfluve samples have ^{10}Be concentrations in excess of what is predicted for saturated samples. The point of 'saturation' with respect to a specific radionuclide describes the maximum concentration a sample can reach before the rate of radionuclide loss by decay matches the rate of production. Higher rates of production correspond to a greater saturation concentration. Conversely, if the surface of the sample is eroding the point of saturation will correspond to a lower concentration. Using the production rates we calculated for Pampa de Tana, the saturation

concentration assuming zero erosion of the samples is indicated on Figures 7A and 7B by the small circle marking the tip of the steady-state erosion island. A 22% production rate increase would be needed to resolve the excess ^{10}Be observed in Figure 7A.

<<Approximate location of figure 7 >>

Given that our fluvially deposited samples derived from higher elevations, any ^{10}Be or ^{26}Al inherited during erosion of the samples out of the parent bedrock and their storage or transport prior to reaching Pampa de Tana would assume a higher rate of production. We can consider this in regard to the oversaturated samples plotted in Figure 7A that, using the LSD production rate scaling, have a ^{10}Be concentration excess of at least 3×10^6 at/g, relative to the precision of the measurements. The minimum age we estimate for the saturated samples is 5.6 Myr and accounting for the radionuclide decay over this period would mean that, if the excess ^{10}Be derives from a higher elevation, the samples must have been deposited at their modern locations with a ^{10}Be concentration of 49×10^6 at/g. The corresponding excess of ^{26}Al in the samples when they were deposited on Pampa de Tana would approximate seven times that of ^{10}Be , with the exact value depending on the elevation history of the samples (Lifton et al., 2014), but after 5.6 Myr of more rapid decay the excess ^{26}Al concentration is about half the excess of ^{10}Be . We can examine what scenarios of upstream erosion rate and transport/storage would allow the amounts of ^{10}Be oversaturation we find in the Pampa de Tana samples. For example, erosion of the clasts from bedrock at a rate of 0.1 m/Myr and an elevation of 3500 m and then subsequent surface exposure at this elevation for 400 kyr, before transport to the lower elevations of Pampa de Tana at 5.6 Myr ago, would result in a ^{10}Be concentration of approximately 49×10^6 at/g. This is enough to produce the oversaturation we observe in Figure 7A but

such low erosion rates would be surprising for a mountainous region. Increasing the rate of erosion requires either a longer subsequent exposure time at this elevation, or that the upstream catchment source area was more elevated, or both. Clasts brought to the surface by erosion rates of 10 m/Myr at 4000 m elevation would require subsequent exposure for 2.2 Myr before being transported downstream in order to attain the excess ^{10}Be concentrations evident in figure 7A. Such a scenario is feasible if the clasts had originated from, for instance, an intermontane Andean valley, but these scenarios also assume zero erosion of the clast surfaces after they have eroded out of the bedrock.

A combination of production at higher elevations and underestimated production rates at our site can explain the oversaturated samples shown in Figure 7. However, three samples (TA1A, TA1B and TA5A) have ^{10}Be concentrations exceeding 20×10^6 at/g (Table 1). These do not appear in Figure 7, as ^{26}Al was not determined on these samples. Resolving oversaturation of ^{10}Be that reaches concentrations of 25×10^6 at/g (TA5A) using production at high elevations alone would require saturation of non-eroding clasts at 5500 m before transport and deposition at Pampa de Tana. As this scenario is unlikely it points to either more significant production rate underestimates, or issues during sample preparation/measurement. However, we note oversaturated samples measured from similar elevations in northern Chile have also been reported by other groups (Nishiizumi et al., 2011).

Accounting for uncertainties, none of our samples have experienced sufficient burial to resolutely place them in the zone of complex exposure, although this assertion is less clear for some of the oversaturated samples (Figure 7A and 7B). The measurement of ^{10}Be and ^{26}Al in stream sediments from the currently active Quebrada de Camiña, which contains flowing water (site 6, Table 1), gives a ^{10}Be concentration that is at least an order magnitude less than the concentrations recorded at all sites except the southern channel, where it is approximately half as much as the lowest concentration (Table 1; see Figures 3 and 6 for the location of the southern channel with respect to Quebrada de Camiña). This suggests the fluvial sediments in the Quebrada de Camiña are eroded and transported rapidly

enough to prevent significant pre-exposure concentrations, or 'inheritance', of ^{10}Be and ^{26}Al , relative to the million-year ages we typically observe here. In some of the samples from the southern paleochannel we measure concentrations of ^{10}Be and ^{26}Al that are comparable to that found in the active channel of the Quebrada de Camiña, meaning the southern channel might have been recently active. However, the modern stream sample (site 6) is not a direct analogy for our channel sites, being a finer grain size and coming from a more incised channel draining a larger catchment, characteristics that might result in concentration differences (Codilean et al., 2014). Additionally, the ranges of the ages in the central and southern channels are indicative of significant, million-year equivalent pre-exposure. We suggest, in the absence of evidence for burial, that the youngest age of 2.0 Myr for the abandonment of the central channel is the most reliable and that older ages have experienced notable pre-exposure. Similarly the southern channel has likely been active in the last 100 kyr, after inheritance is accounted for.

4.3. ^{21}Ne results

The neon isotope composition of all samples and CREU standards are shown in Figures 8A and 8B. Samples NTA1D, NTA4D and NTA5D plot above the air-spallation mixing line indicative of a contribution non-cosmogenic Ne present in the quartz samples. The concentration of ^{21}Ne in these samples is an upper limit on their exposure history. Cosmogenic ^{21}Ne concentrations and exposure ages are reported in Table 1 and Table 2.

<<Approximate location of figure 8 >>

The ^{21}Ne concentrations give ages that range from 1.4 to 8.3 Myr for the northern channel (site 1), 1.1 to 2.4 Myr for the central channel and 0.4 Myr for the southern channel. Ages for the interfluves range from 2.6 to 8.2 Myr. The overall pattern of decreasing channel ages southwards and older ages on the interfluves that is observed with ^{10}Be and ^{26}Al is preserved. However, nine of the twelve ^{21}Ne ages are younger (within 2 standard deviations) than predicted by ^{10}Be or ^{26}Al concentrations. Davis et al. (2011) find that cosmogenic ^{21}Ne loss from chert-rich samples from near the Dead Sea in Israel can explain younger than predicted ^{21}Ne ages. From south of our fieldsite, but still in the hyperarid Atacama Desert, Placzek et al. (2010) plot a single $^{21}\text{Ne}/^{10}\text{Be}$ result that suggests loss of ^{21}Ne . Furthermore, cosmogenic ^3He in pyroxene from boulders from a site that should be contemporaneous with our interfluve samples gave exposure ages of 11 – 20 Myr (Evenstar et al. 2017), much greater than our ^{21}Ne ages from the interfluves of 2.3 – 8.2 Myr, but in keeping with the uniformly saturated results from ^{10}Be measurements. The Raman Spectrometry measurements of a subset of the samples and visual inspections during crushing show that they most likely contain microcrystalline quartz. On the basis of the diffusive parameters determined by Shuster and Farley (2005), it is possible that the diffusive loss of cosmogenic ^{21}Ne from fine grained quartz at Atacama Desert temperatures can explain the apparent discrepancy between the ^{10}Be and ^{21}Ne exposure ages. Consequently we focus our below discussion on the ages obtained from ^{10}Be and ^{26}Al .

4.4. Channel profiles and topographic analysis

The swath approach used gives both the channel profile and a profile of the maximum elevations adjacent to the channel, i.e. the channel bank. Channel profiles and channel-bank profiles for the northern, central and southern channels are shown in Figure 9 (see also Supplementary Data). The northern and central channels show convexities in their profiles suggesting they became abandoned and

have since been warped upwards due to local uplift. These malformations of the channel profiles occur where they cross the eastern scarp (Figure 3A). The northern channel profile exhibits two such channel convexities, the second instance being 4 km west of the first one. The profile of the northern channel is also approximately mirrored in the profile of the adjacent channel-bank, suggesting the local relief on the surface of the topographic bulge proximal to the northern channel is due to uplift rather than erosion. This seems reasonable, as the channel appears to follow the trace of a monocline (Garcia et al., 2013) (Figure 3C). Aside from the deformation of the channel profile where it crosses the eastern scarp, the central channel profile maintains a generally more linear form than the northern channel. However, the channel-bank profile of the central channel shows a second topographic high around 4 km west of the eastern scarp. That this deformation is not evident in the channel profile suggests this uplift predates that associated with the eastern scarp and fluvial incision was rapid enough to keep pace with this earlier uplift. The southern channel has a linear profile that is not malformed as it passes through the eastern scarp, providing evidence that incision has kept pace with uplift and the channel can maintain flow, as supported by the relatively young ages reported in section 4.1.

The height of the eastern scarp is greatest between the northern and central channels where it reaches around 40 m and lowers near the southern channel where it is around 10 m (Figure 9). The scarp appears to be comprised of several short, slightly offset, sections that are steepest around the central channel and shallowest around the northern channel (Figure 3A). Clay deposits are found along the base of the scarp and a claypan several kilometers across has formed in a shallow depression in front of the scarp to the north (Figure 3B). The claypan appears fed by small streams flowing from the north, east as well as from the south, parallel to the scarp, suggesting the rerouting and ponding of streams relating to the formation of the scarp.

<<Approximate location of figure9 >>

5. History of channel abandonment, rates of uplift and rates of fluvial incision

Our cosmogenic ^{10}Be and ^{26}Al exposure ages show the northern channel (Figure 6) became abandoned before the central and southern channels, sometime before 5.6 Myr ago, with a maximum age constrained by the 11 Myr age of the El Diablo Formation (see section 2.1). The central channel appears to have been active 2 Myr ago. The most southerly channel has seen fluvial activity in at least the last few hundred thousand years and probably more recently. Although the individual ages at each of the three channel sites show scatter, there is a clear difference between the timing of abandonment of the sites. All samples in the northern channel are saturated with respect to ^{10}Be , the central channel shows a mixture of saturated samples and ages on the order of millions of years, while the southern channel has no samples saturated with respect to either ^{10}Be or ^{26}Al , and mostly hundred thousand year ages. In short, the ages suggest stream abandonment moved progressively south.

Ages of abandonment of the northern and central channels, combined with the channel profiles, allows us to place constraints on the average rate of vertical uplift of the topographic bulge that has occurred since the streams were defeated. In order to gauge the total amount of vertical uplift we need to estimate what form the channels would have if the streams had not been blocked. For this we assume simplified, linear channel profiles from where they meet the eastern scarp to the point downstream where the degree of incision is minimal and presumably any influence of uplift has waned. This form is similar to what we currently see in the southern channel (Figure 9) and is termed the 'no-uplift' profile in Figure 10. The differences of elevation between the channel profile and the no-uplift profile gives the amount of vertical displacement that has occurred since channel abandonment. We then use our chronology of channel abandonment to estimate a rate of vertical uplift, averaging over the last 5.6 Myr

in the case of the northern channel and the last 2 Myr in the case of the central channel (Figure 10). We find that the uplift of the northern channel reaches $\sim 8\text{m/Myr}$, while in the central channel our estimates reach $\sim 12\text{ m/Myr}$ in places. We do not attempt to formally ascribe uncertainties to these rates given that the sources of uncertainty, including the timing of channel abandonment and form the channel would take in the absence of uplift are difficult to assess. However, the likely precision of our uplift rate estimates are such that the rates averaged over 2.0 Myr in the central part of the uplifted topographic bulge are comparable to those in the north over timescales of 5.6 Myr. If the abandonment of the northern channel was significantly earlier than our 5.6 Myr minimum, rates in the north might be low enough to discriminate from those of the central channel.

<<Approximate location of figure 10 >>

In addition to the rates of uplift after abandonment of the channels, we can obtain estimates for the rates of fluvial incision before abandonment. To do this we recognize the channels have incised into the preserved surface of the El Diablo Formation and that we can use the 11 Myr estimate for when this surface became stable as a marker horizon (section 2.2). The total depth of incision is given by the difference in elevation between the channel-bank profile (i.e. the surface of the El Diablo Formation adjacent to the channel) and the channel profile (Figure 9). The rate of incision is then obtained by averaging this depth over the time between the end of the El Diablo Formation and the abandonment of the channels (Figure 10). Thus, we obtain fluvial incision rates for the northern channel of 4 m/Myr , during the period from 11 Myr to 5.6 Myr. Rates of fluvial incision are less than 3 m/Myr for the central and southern channels, during the periods from 11 Myr to 2 Myr, and the last 11 My, respectively. It should be noted that, like the rates of uplift described earlier, these incision rates are averaged over a

significant period of time. Actual rates of incision are probably much higher over the short term, separated by periods of stability and perhaps also aggradation. This type of non-equilibrium fluvial operation is especially true of ephemeral streams in desert environments (Powell, 2009). In addition, this approach to quantify uplift and incision is complicated by the uncertainty in when the El Diablo Formation ceased to aggrade, and by our swath approach to determine the channel-bank elevation that might incorporate higher topography some distance from the channel itself. None-the-less, the picture that emerges from this attempt to compare uplift and incision rates is one where uplift rates averaged over the period of time since streams were defeated appear to be greater than preceding rates of fluvial incision.

6. Discussion

6.1. Concurrent preservation and evolution of the Atacama landscape

^{10}Be saturation of all the interfluvial samples (sites 4 and 5, Table 2, Figure 3D) is evidence that these surfaces are stable, with minimal clast erosion and turbation of the surface regolith. This notion of interfluvial stability is in good agreement with the >11Myr age Evenstar et al. (2017) find using ^3He at a location close to our sites and from the same depositional surface. Saturation of our interfluvial samples and corresponding $^{26}\text{Al}/^{10}\text{Be}$ ratios are generally consistent with a period of exposure where there has been minimal burial and/or clast erosion. More precise constraints on the position of the steady-state erosion island on the two-isotope diagram (Figures 7A and 7B), or depth profiles (e.g. Davis et al., 2014; Jungers et al., 2013) would be needed to find strong evidence for any shallow or slowly operating regolith processes.

There is a sharp contrast in ^{10}Be concentrations, and hence ages, between the most recently active, southern channel and the adjacent interfluvial (sites 3 and 4 on Table 1, Figure 6). These sites are

approximately 100 m apart and the channel is incised only a few meters into this surface. There are two implications of this contrast. Firstly, there is no evidence for transport of clasts over short distances from the flat interfluvies into the channels, again indicating the stability of this surface, at least in the case of cm sized pebbles. Secondly, interfluvies that have undergone minimal modification since the Miocene exist adjacent to shallowly incised channels that show evidence for much more recent fluvial activity (likely within the last 100 kyr in the case of the southern channel). The origins and evolution of different geomorphological features within this landscape are thus governed by processes operating over very different timescales. Precipitation that has fallen on Pampa de Tana since at least the Late Miocene appears not to have been sufficient to have removed clasts that have existed at, or close to, the gypsum dust mantled surfaces of the conglomeratic El Diablo Formation. Jordan et al. (2014) note that the location or geomorphic feature under consideration may be a contributing factor to the disagreement between several studies attempting to constrain the timing of hyper-aridification within the Atacama Desert. Our results reiterate the point that the source of fluvial deposits as proxies in this debate need to be carefully considered, as do other extrinsic tectonic and intrinsic geomorphic mechanisms influencing such proxies and these are discussed in more detail below.

6.2. Causes of channel abandonment

Given that we find progressively younger ages of channel abandonment southwards it is tempting to ascribe the directional forcing of drainage around uplifting topography as the cause, as recorded elsewhere (e.g. Burbank et al., 1996; Medwedeff et al., 1992), and in the results of modelling studies (Tomkin and Braun, 1999). However, the topographic profile along the scarp at the leading edge of the uplift (Figure 9) shows the surface of Pampa de Tana upstream of the scarp is tilted downward towards the north, as can also be seen by the lower elevations of the channels in the north compared to the

south (Figure 8). This effect of lower northern channels is due to the orientation of the topographic bulge in a north-west to south-east direction on a west facing slope, meaning the scarp at the northwestern end is at a lower elevation when compared to the southeastern end. This also means that drainages could not be forced south as they were blocked by growing topography and as such the drainages crossing the anticline were antecedent and then superposed as the surface uplifted. That these channels did not develop more significant low order tributaries and widen their catchments via headward erosion of those tributaries where they incised the uplifting bulge further suggests any precipitation that has fallen on Pampa de Tana since the beginning of uplift, at least as far back as 5.6 Myr ago, has had minimal influence shaping this surface. Our long-term average fluvial incision and uplift rates (Figure 10, section 5) suggest uplift rates since abandonment of the northern channel over the last >5.6 Myr and abandonment of the central channel over the last 2 Myr were greater than the preceding rates of fluvial incision. This is particularly apparent on the central channel, where our estimates of uplift over the last 2 Myr reach rates six-fold greater than preceding fluvial incision. Though there are several broad assumptions included in these rate derivations, we propose uplift has been the first order control of channel avulsion.

Incision of the southern channel has been able to keep pace with the displacement rates of the scarp. This might relate to lower uplift rates in the southeast. The southern channel also flows into the deeper incised Quebrada de Camiña downstream of the anticline and this connection to a lower local base-level could have driven more rapid incision and helped it maintain its course through the uplifting scarp. However, there appears to be little incision of the reach lying upstream of the point where the southern channel joins the trunk of the quebrada (Figure 3A), suggesting the influence of this lower local base-level has not propagated upstream in the southern channel as far as the area of topographic uplift. Abandonment of the northern and central but not the southern channels could also relate to consumption of the Pampa de Tana surface, where lateral expansion of the Quebrada de Camarones to

the north has annexed the catchment areas feeding the northern and central channels more so than has occurred in the south. It is clear from satellite imagery of the area upstream of the topographic bulge that capture of the pampa drainages is ongoing and the narrow apex at the highest point of Pampa de Tana, where access to discharge from higher elevations has been cut-off, is the result of the headward and lateral expansion of the quebradas (Figure 11). Similar drainage capture of older streams by more recent, large canyon incision is observed north of Pampa de Tana (García and Hérail, 2005; Hoke et al., 2004). The notion that capture has been more prevalent for northern Pampa de Tana drainages than southern ones agrees with the general picture of quebrada evolution, whereby incision of the Quebrada de Camarones into the Central Depression occurred around 13-12 Myr ago, while Quebrada de Camiña (Quebrada de Tana) connected to the sea later, incising through the Coastal Cordillera 7-5 Myr ago (Evenstar et al, 2017; Farías et al., 2005, Naranjo and Paskoff, 1985) and downcutting significantly into the Central Depression perhaps only the last 3 Myr (Kirk-Lawler et al., 2013). More lateral expansion of the Quebrada de Camarones may be occurring via the large landslides reported for its tributaries (Garcia et al., 2011; Pinto et al., 2008; Crosta et al., 2014). Here, we suggest that the removal of the upstream catchment area by the headward erosion of the large bounding quebradas, especially to the north, has reduced the discharge of the streams flowing over the pampa and diminished their ability to keep pace with the rate of uplift of the eastern scarp, either due to having less stream power or transporting less sediment to the base of the scarp. This effect is less pronounced in the south and may have allowed the southern channel to keep pace with uplift.

<<Approximate location of figure 11 >>

6.3. Broader implications of drainage adaptation

6.3.1. Tectonic interpretation

The chronology of evolution of the three channels on top of a tectonically raised bulge gives some insights into the active tectonic processes during the Neogene (Pliocene) in northern Chile. Presumably, these channels formed directly after the formation of the Pampa de Tana surface, which itself formed as result of the regional uplifting of the Precordillera and the subsequent aggradation processes linked with the infill of the Central Depression since the Oligocene (Azapa Formation, Salas et al., 1966), ending with the deposition of the El Diablo Formation during the Miocene. The asymmetric profile of the topographic bulge, characterized by a steeper eastern scarp and gentler western scarp is interpreted as the surface expression of fault propagation folding above a west-dipping blind reverse fault forming the anticline depicted in Figure 3c. We used cross-sectional topographic profiles of the channels and channel banks (Figure 9) as well as the Pampa de Tana surface (Figure 6) as morphological markers to reconstruct the uplift and anticlinal bending, which could best be reproduced by reverse faulting. Although there is no direct information about the fault geometry at depth, normal faulting for the formation of the observed structure can be excluded due to the shape of the surface traces of the scarps located at the western and eastern limbs of the anticline. Their convex shape with regard to the topographic scarps require an east dipping fault plane for the western limb and a west dipping fault plane for the eastern limb. Together with the uplift signal this geometry clearly points to a fault propagation fold geometry, well in agreement with other compressional structures along the foothills of the western Altiplano flank south of Pampa Tana (Farias et al. 2005, Munoz & Charrier 1996, Victor et al 2004). The resulting topographic displacement can be followed for 46 km along-strike between Quebrada de Camarones to south of Quebrada de Camiña. Therefore, we suggest that this reverse blind fault is a major structure of the forearc that has been at least in part responsible for the uplift of Pampa de Tana and the Coastal Cordillera at this latitude. This finding demonstrates that the regional Neogene

tectonic regime is in some way dominated by east-west compression, which has constructed a forearc bulge between the western border of the Coastal Cordillera and the Pampa de Tana.

6.3.2. The downstream implications of stream diversion

Our findings show that the pampa surface to the west of the topographic uplift ceased to receive overland channel flow from the east at around 2 Myr ago, when the central channel became abandoned. This assumes the southern channel was draining then, as it does now, into an incised Quebrada de Camiña just downstream of the topographic bulge, and thus not supplying discharge to the western areas of the Pampa de Tana during the last 2 Myr. It seems plausible that the southern channel was draining into the Quebrada de Camiña at this time given that major incision of this quebrada was proposed to have occurred sometime after 3 Myr ago, following the draining of a paleolake that occupied western portions of the pampa (Kirk-Lawler et al. 2013). About 20 – 25 km downstream of the eastern scarp, the Coastal Cordillera forms a topographic barrier to minor westward flowing drainages and there is little evidence for eastward directed flow emanating from the Coastal Cordillera at this latitude. Thus, the tract of land lying between the topographic bulge and the eastern fringe of Coastal Cordillera between the Quebrada de Camarones and Quebrada de Camiña has not received channel flow in the last 2 Myr due to the slow average uplift of a subtle tectonic structure. The geochronological constraints on when drainages were last active in this area make it well suited to studies investigating long-term biological evolution in extreme environments, or to geomorphological studies considering the development of topography in the absence of flowing water in terrestrial and extra-terrestrial landscapes.

7. Conclusions

Preserved remnants of drainages in deserts constitute sensitive indicators of changing boundary conditions and provide a means to estimate rates of tectonic and geomorphological processes.

Topographical analyses shows westward flowing stream networks on Pampa de Tana in the northern Atacama Desert have been blocked by a scarp formed above a blind reverse fault, preserving paleochannels in the uplifted topography. By dating the timing of paleochannel abandonment using cosmogenic nuclides in fluvial sediment deposits we derive a chronology for the long-term evolution of this drainage. While chronological constraints are only broadly defined, we see a clear variation in the timing of channel abandonment that moved progressively south over at least the last 5.6 Myr. The first-order control of the abandonment of the channels that once incised into this uplifted topography appears to be tectonic uplift of a scarp at a rate that averages typically less than ten meters per million years. While relatively slow, this rate of uplift exceeds rates of earlier fluvial incision by several-fold. Upstream drainage capture and the beheading of streams on the pampa, as it was consumed by headward erosion and the lateral expansion of the north and south bounding quebradas, could have played a role in reducing the ability of the paleochannels to traverse the uplifting scarp by reducing their catchment areas and thus lowering the precipitation they receive. The southernmost channel dated here shows relatively recent fluvial activity across a surface of great antiquity that is a testament to the polygenetic nature of the Atacama Desert. This notion of polygenesis, plus the recognition that subtle topographic changes in response to slow rates of tectonic uplift can reroute past stream networks, suggests care is needed when using fluvial records to examine the long-term stability of hyperarid climates in tectonically active regions. Furthermore, we consider that the fault that has driven the channel abandonment extends several tens of km further south of our study area, and constitutes a major east-west compressional structure of the forearc bulge in this region.

Acknowledgements

We thank Elena Voronina, Tomasz Goral, Elaine McDougall and Luigia Di Nicola for assistance in the laboratory. We are grateful to Bennedikt Ritter for acquiring the SPOT-6 imagery and Jorien van der Wal and Jana Mittelstädt for assistance in the field. We are also very grateful to Fernando Sepúlveda and Marcelo García at SERNAGEOMIN for their scientific input, and to Eduardo Campos and Damian Lopez who provided invaluable logistical support. Thoughtful comments made by reviewers Regis Braucher and Vincent Regard resulted in an improved manuscript. We thank Dietmar Quandt for editorial handling. This work was funded in part by the Deutsche Forschungsgemeinschaft (DFG, German Research Foundation) – Projektnummer 268236062 – SFB 1211.

References

- Alpers, C.N. and Brimhall, G.H., 1988. Middle Miocene Climatic-Change in the Atacama Desert, Northern Chile - Evidence from Supergene Mineralization at La-Escondida. *Geological Society of America Bulletin*, 100(10), 1640-1656.
- Amos, C.B., Burbank, D.W. and Read, S.A.L., 2010. Along-strike growth of the Ostler fault, New Zealand: Consequences for drainage deflection above active thrusts. *Tectonics*, 29.
- Amundson, R. et al., 2012. Geomorphologic evidence for the late Pliocene onset of hyperaridity in the Atacama Desert. *Geological Society of America Bulletin*, 124(7-8), 1048-1070.
- Balco, G., 2017. Production rate calculations for cosmic-ray-muon-produced Be-10 and Al-26 benchmarked against geological calibration data. *Quaternary Geochronology*, 39, 150-173.
- Balco, G., Stone, J.O., Lifton, N.A. and Dunai, T.J., 2008. A complete and easily accessible means of calculating surface exposure ages or erosion rates from Be-10 and Al-26 measurements. *Quaternary Geochronology*, 3(3), 174-195.
- Blanco, N. and Tomlinson, A.J., 2013. Carta Guatacondo, Región de Tarapacá, Serie Geología Basica 15, 109. Nacional de Geología y Minería, Subdirección Nacional de Geología, Carta Geológica de Chile, Santiago, Chile.
- Binnie, S.A. et al., 2019. Preliminary results of CoQtz-N: A quartz reference material for terrestrial in-situ cosmogenic ^{10}Be and ^{26}Al measurements.
- Binnie, S.A. et al., 2015. Separation of Be and Al for AMS using single-step column chromatography. *Nuclear Instruments & Methods in Physics Research Section B-Beam Interactions with Materials and Atoms*, 361, 397-401.

Binnie, S.A., Phillips, W.M., Summerfield, M.A. and Fifield, L.K., 2007. Tectonic uplift, threshold hillslopes, and denudation rates in a developing mountain range. *Geology*, 35(8), 743-746.

Borchers, B. et al., 2016. Geological calibration of spallation production rates in the CRONUS-Earth project. *Quaternary Geochronology*, 31, 188-198.

Burbank, D.W., Meigs, A. and Brozović, N., 1996. Interactions of growing folds and coeval depositional systems. *Basin Research*, 8, 199-223.

Carrizo, D., González, G.A. and Dunai, T.J., 2008. Constricción neógena en la Cordillera de la Costa, norte de Chile: neotectónica y datación de superficies con ^{21}Ne cosmogónico. *Revista Geológica de Chile*, 35(1), 1-38.

Charrier, R. et al., 2013. Cenozoic tectonic evolution in the Central Andes in northern Chile and west central Bolivia: implications for paleogeographic, magmatic and mountain building evolution. *International Journal of Earth Sciences*, 102(1), 235-264.

Chmeleff, J., von Blanckenburg, F., Kossert, K. and Jakob, D., 2010. Determination of the Be-10 half-life by multicollector ICP-MS and liquid scintillation counting. *Nuclear Instruments & Methods in Physics Research Section B-Beam Interactions with Materials and Atoms*, 268(2), 192-199.

Codilean, A.T. et al., 2008. Single-grain cosmogenic Ne-21 concentrations in fluvial sediments reveal spatially variable erosion rates. *Geology*, 36(2), 159-162.

Codilean, A.T., Fenton, C.R., Fabel, D., Bishop, P. and Xu, S., 2014. Discordance between cosmogenic nuclide concentrations in amalgamated sands and individual fluvial pebbles in an arid zone catchment. *Quaternary Geochronology*, 19, 173-180.

Collignon, M., Yamato, P., Castellort, S. and Kaus, B.J.P., 2016. Modeling of wind gap formation and development of sedimentary basins during fold growth: application to the Zagros Fold Belt, Iran. *Earth Surface Processes and Landforms*, 41(11), 1521-1535.

Crosta, G.B., Hermanns, R., Frattini, P., Valbuzzi, E. and Valagussa, A., 2014. Large Slope Instabilities in Northern Chile: Inventory, Characterization and Possible Triggers. In: S. K., C. P. and Y. Y. (Eds.), *Landslide Science for a Safer Geoenvironment*. Springer.

Davis, M., Matmon, A., Placzek, C., McIntosh, W., Rood, D.H. and Quade, J., 2014. Cosmogenic nuclides in buried sediments from the hyperarid Atacama Desert, Chile. *Quaternary Geochronology*, 19, 117-126.

Davis, M., Matmon, A., Fink, D., Ron, H. and Niedermann, S., 2011. Dating Pliocene lacustrine sediments in the central Jordan Valley, Israel - Implications for cosmogenic burial dating. *Earth and Planetary Science Letters*, 305(3-4), 317-327.

Dewald, A. et al., 2013. CologneAMS, a dedicated center for accelerator mass spectrometry in Germany. *Nuclear Instruments & Methods in Physics Research Section B-Beam Interactions with Materials and Atoms*, 294, 18-23.

Dunai, T.J., Lopez, G.A.G. and Juez-Larre, J., 2005. Oligocene-Miocene age of aridity in the Atacama Desert revealed by exposure dating of erosion-sensitive landforms. *Geology*, 33(4), 321-324.

Evenstar, L.A. et al., 2009. Multiphase development of the Atacama Planation Surface recorded by cosmogenic He-3 exposure ages: Implications for uplift and Cenozoic climate change in western South America. *Geology*, 37(1), 27-30.

Evenstar, L.A. et al., 2017. Geomorphology on geologic timescales: Evolution of the late Cenozoic Pacific paleosurface in Northern Chile and Southern Peru. *Earth-Science Reviews*, 171, 1-27.

Farias, M., Charrier, R., Comte, D., Martinod, J. and Herail, G., 2005. Late Cenozoic deformation and uplift of the western flank of the Altiplano: Evidence from the depositional, tectonic, and geomorphologic evolution and shallow seismic activity (northern Chile at 19 degrees 30 ' S). *Tectonics*, 24(4).

García, M., Fuentes, G. and Riquelme, F., 2013. Carta Miñimiñi, Regiones de Arica y Parinacota y de Tarapacá., Carta Geológica de Chile, Serie Geología Básica 157: p., 1. Servicio Nacional de Geología y Minería, Santiago.

Garcia, M. and Herail, G., 2005. Fault-related folding, drainage network evolution and valley incision during the Neogene in the Andean Precordillera of Northern Chile. *Geomorphology*, 65(3-4), 279-300.

Garcia, M., Riquelme, R., Farias, M., Herail, G. and Charrier, R., 2011. Late Miocene-Holocene canyon incision in the western Altiplano, northern Chile: tectonic or climatic forcing? *Journal of the Geological Society*, 168(4), 1047-1060.

Hampel, A. and Hetzel, R., 2016. Role of climate changes for wind gap formation in a young, actively growing mountain range. *Terra Nova*, 28(6), 441-448.

Hartley, A.J., 2003. Andean uplift and climate change. *Journal of the Geological Society*, 160, 7-10.

Hartley, A.J. and Chong, G., 2002. Late Pliocene age for the Atacama Desert: Implications for the desertification of western South America. *Geology*, 30(1), 43-46.

Heaney, P.J. and Post, J.E., 1992. The Widespread Distribution of a Novel Silica Polymorph in Microcrystalline Quartz Varieties. *Science*, 255(5043), 441-443.

Hoke, G.D., Isacks, B.L., Jordan, T.E. and Yu, J.S., 2004. Groundwater-sapping origin for the giant quebradas of northern Chile. *Geology*, 32(7), 605-608.

Houston, J. and Hartley, A.J., 2003. The central andean west-slope rainshadow and its potential contribution to the origin of HYPER-ARIDITY in the Atacama desert. *International Journal of Climatology*, 23(12), 1453-1464.

Humphrey, N.F. and Konrad, S.K., 2000. River incision or diversion in response to bedrock uplift. *Geology*, 28(1), 43-46.

Isacks, B.L., 1988. Uplift of the Central Andean Plateau and Bending of the Bolivian Orocline. *Journal of Geophysical Research-Solid Earth and Planets*, 93(B4), 3211-3231.

Jackson, J., Norris, R. and Youngson, J., 1996. The structural evolution of active fault and fold systems in central Otago, New Zealand: Evidence revealed by drainage patterns. *Journal of Structural Geology*, 18(2-3), 217-&.

Jansen, J.D. et al., 2013. Lowland river responses to intraplate tectonism and climate forcing quantified with luminescence and cosmogenic Be-10. *Earth and Planetary Science Letters*, 366, 49-58.

Jordan, T.E., Kirk-Lawlor, N.E., Blanco, N., Rech, J.A. and Cosentino, N.J., 2014. Landscape modification in response to repeated onset of hyperarid paleoclimate states since 14 Ma, Atacama Desert, Chile. *Geological Society of America Bulletin*, 126(7-8), 1016-1046.

Jordan, T.E. et al., 2010. Uplift of the Altiplano-Puna plateau: A view from the west. *Tectonics*, 29.

Jungers, M.C. et al., 2013. Active erosion-deposition cycles in the hyperarid Atacama Desert of Northern Chile. *Earth and Planetary Science Letters*, 371, 125-133.

Keller, E.A., Zepeda, R.L., Rockwell, T.K., Ku, T.L. and Dinklage, W.S., 1998. Active tectonics at Wheeler Ridge, southern San Joaquin Valley, California. *Geological Society of America Bulletin*, 110(3), 298-310.

Kirk-Lawlor, N.E., Jordan, T.E., Rech, J.A. and Lehmann, S.B., 2013. Late Miocene to Early Pliocene paleohydrology and landscape evolution of Northern Chile, 19 degrees to 20 degrees S.

Palaeogeography Palaeoclimatology Palaeoecology, 387, 76-90.

Kober, F. et al., 2007. Denudation rates and a topography-driven rainfall threshold in northern Chile: Multiple cosmogenic nuclide data and sediment yield budgets. Geomorphology, 83(1-2), 97-120.

Kohl, C.P. and Nishiizumi, K., 1992. Chemical Isolation of Quartz for Measurement of Insitu-Produced Cosmogenic Nuclides. Geochimica Et Cosmochimica Acta, 56(9), 3583-3587.

Korschinek, G. et al., 2010. A new value for the half-life of Be-10 by Heavy-Ion Elastic Recoil Detection and liquid scintillation counting. Nuclear Instruments & Methods in Physics Research Section B-Beam Interactions with Materials and Atoms, 268(2), 187-191.

Lifton, N., Sato, T. and Dunai, T.J., 2014. Scaling in situ cosmogenic nuclide production rates using analytical approximations to atmospheric cosmic-ray fluxes. Earth and Planetary Science Letters, 386, 149-160.

Medwedeff, D., 1992. Geometry and Kinematics of an Active, Laterally Propagating Wedge Thrust, Wheeler Ridge, California. In: S. Mitra and G.W. Fisher (Eds.), Structural Geology of Fold and Thrust Belts. John Hopkins University Press, Baltimore.

Mortimer, C., 1980. Drainage evolution in the Atacama Desert of Northern Chile. Revista Geológica de Chile, 11, 3-28.

Mortimer, C. and Saric, N., 1975. Cenozoic studies in northernmost Chile. Geologische Rundschau, 64, 395-420.

Mortimer, C., Farrar, E. and Saric, N., 1974. K-Ar ages from Tertiary lavas of the northernmost Chilean Andes. *Geologische Rundschau*, 63, 484 - 489.

Mortimer, C. and Saric, N., 1972. Landform Evolution in the Coastal Region of Tarapaca Province, Chile. *Revue de Geomorphologie Dynamique*, 21, 162-170.

Muñoz, N. and Charrier, R., 1996. Uplift of the western border of the Altiplano on a west-vergent thrust system, Northern Chile. *Journal of South American Earth Sciences*, 9(3-4), 171-181.

Muñoz, N. and Sepúlveda, S.A., 1992. Estructuras compresivas con vergencia al oeste en el borde oriental de la Depresión Central, Norte de Chile (19°15'S). *Revista Geológica de Chile*, 19(2), 241-247.

Naranjo, J.A. and Paskoff, R., 1985. Evolución cenozoica del piedemonte andino en la Pampa del Tamarugal, norte de Chile (18°-21°S). 4th Congreso Geológico Chileno, University Catolica del Norte, Antofagasta, Chile.

Nishiizumi, K., 2004. Preparation of Al-26 AMS standards. *Nuclear Instruments & Methods in Physics Research Section B-Beam Interactions with Materials and Atoms*, 223, 388-392.

Nishiizumi, K. et al., 2011. Long-Term Production Rates of Cosmogenic Nuclides: Millions of Years of Rock Exposure in Antarctica and the Atacama Desert. *Mineralogical Magazine*, 75(3), 1543.

Nishiizumi, K., Caffee, M.W., Finkel, R.C., Brimhall, G. and Mote, T., 2005. Remnants of a fossil alluvial fan landscape of Miocene age in the Atacama Desert of northern Chile using cosmogenic nuclide exposure age dating. *Earth and Planetary Science Letters*, 237(3-4), 499-507.

Nishiizumi, K. et al., 2007. Absolute calibration of Be-10 AMS standards. *Nuclear Instruments & Methods in Physics Research Section B-Beam Interactions with Materials and Atoms*, 258(2), 403-413.

Oerter, E. et al., 2016. Early to Middle Miocene climate in the Atacama Desert of Northern Chile.

Palaeogeography Palaeoclimatology Palaeoecology, 441, 890-900.

Ouchi, S., 1985. Response of Alluvial Rivers to Slow Active Tectonic Movement. Geological Society of America Bulletin, 96(4), 504-515.

Pearce, S.A., Pazzaglia, F.J. and Eppes, M.C., 2004. Ephemeral stream response to growing folds.

Geological Society of America Bulletin, 116(9-10), 1223-1239.

Perez-Pena, J.V. et al., 2017. SwathProfiler and NProfiler: Two new ArcGIS Add-ins for the automatic extraction of swath and normalized river profiles. Computers & Geosciences, 104, 135-150.

Pinto, L., Hérail, G. and Charrier, R., 2004. Sedimentación sintectónica asociada a las estructuras neógenas en la Precordillera de la zona de Moquella, Tarapacá (19°15'S, norte de Chile). Revista Geológica de Chile, 31, 19-44.

Pinto, L., Hérail, G., Sepulveda, S.A. and Krop, P., 2008. A Neogene giant landslide in Tarapaca, northern Chile: A signal of instability of the westernmost Altiplano and palaeoseismicity effects. Geomorphology, 102(3-4), 532-541.

Placzek, C.J., Matmon, A., Granger, D.E., Quade, J. and Niedermann, S., 2010. Evidence for active landscape evolution in the hyperarid Atacama from multiple terrestrial cosmogenic nuclides. Earth and Planetary Science Letters, 295(1-2), 12-20.

Powell, M.D., 2009. Dryland Rivers: Processes and Forms. In: A.J. Parsons and A.D. Abrahams (Eds.), Geomorphology of Desert Environments. Springer.

Reid, I., 2009. River Landforms and Sediment: Evidence of Climatic Change. In: A.J. Parsons and A.D. Abrahams (Eds.), Geomorphology of Desert Environments. Springer.

Ritter, B. et al., 2018a. Neogene fluvial landscape evolution in the hyperarid core of the Atacama Desert. *Scientific Reports*, 8.

Ritter, B., Binnie, S.A., Stuart, F.M., Wennrich, V. and Dunai, T.J., 2018b. Evidence for multiple Plio-Pleistocene lake episodes in the hyperarid Atacama Desert. *Quaternary Geochronology*, 44, 1-12.

Ritter, B. et al., 2019. Climatic fluctuations in the hyperarid core of the Atacama Desert during the past 215 ka. *Scientific Reports*, 9.

Saez, A. et al., 2012. The stratigraphic record of changing hyperaridity in the Atacama desert over the last 10 Ma. *Earth and Planetary Science Letters*, 355, 32-38.

Schmidt, P., Bellot-Gurlet, L., Slodczyk, A. and Frohlich, F., 2012. A hitherto unrecognised band in the Raman spectra of silica rocks: influence of hydroxylated Si-O bonds (silanole) on the Raman moganite band in chalcedony and flint (SiO₂). *Physics and Chemistry of Minerals*, 39(6), 455-464.

Schumm, S.A., Dumont, J.F. and Holbrook, J.M., 2000. *Active Tectonics and Alluvial Rivers*. Cambridge.

Shuster, D.L. and Farley, K.A., 2005. Diffusion kinetics of proton-induced Ne-21, He-3, and He-4 in quartz. *Geochimica Et Cosmochimica Acta*, 69(9), 2349-2359.

Sobel, E.R., Hilley, G.E. and Strecker, M.R., 2003. Formation of internally drained contractional basins by aridity-limited bedrock incision. *Journal of Geophysical Research-Solid Earth*, 108(B7).

Tomkin, J.H. and Braun, J., 1999. Simple models of drainage reorganisation on a tectonically active ridge system. *New Zealand Journal of Geology and Geophysics*, 42(1), 1-10.

Tooth, S., 2013. Dryland fluvial environments: assessing distinctiveness and diversity from a global perspective. In: E. Wohl (Ed.), *Treatise on Geomorphology*. Academic Press, San Diego, CA pp. 612-644.

Tooth, S., 2012. Arid geomorphology: Changing perspectives on timescales of change. *Progress in Physical Geography-Earth and Environment*, 36(2), 262-284.

Vandenberghe, J., 2003. Climate forcing of fluvial system development: an evolution of ideas. *Quaternary Science Reviews*, 22(20), 2053-2060.

Vermeesch, P. et al., 2015. Interlaboratory comparison of cosmogenic Ne-21 in quartz. *Quaternary Geochronology*, 26, 20-28.

Victor, P., Oncken, O. and Glodny, J., 2004. Uplift of the western Altiplano plateau: Evidence from the Precordillera between 20 degrees and 21 degrees S (northern Chile). *Tectonics*, 23(4).

von Rotz, R., Schlunegger, F., Heller, F. and Villa, I., 2005. Assessing the age of relief growth in the Andes of northern Chile: Magneto-polarity chronologies from Neogene continental sections. *Terra Nova*, 17(5), 462-471.

Figure captions

Figure 1A the coast of northern Chile showing the main topographical domains and large scale drainage patterns. **1B** the study area of Pampa de Tana is located in the red box between the Quebrada de Camarones and Quebrada de Camiña.

Figure 2A shows the geology of the Pampa de Tana region adapted from Herrera et al. (2017), illustrating the distribution of the El Diablo Formation (EDF) discussed in the main text. Extent is the same as in Figure **1B**. MB is the metamorphic basement of the Coastal Cordillera; AOAF is the Azapa, Oxaya and Altos de Pica Formations; LCF is the Lupica and Chucal Formations. Black lines bisecting red boxes are the respective centers and widths of swath profiles shown in the panels beneath. The boxes 11A and 11B refer to the areas covered in Figure **11** (see text for details). The blue dashed box is the area covered by SPOT-6 imagery for which DEM data was derived (see Figures **3** and **6**). The grey and white points show the positions of the photos of Figures **4A** and **4B**, respectively. The swath profile **B-B'** shows the smooth downslope, low relief form of the pediment is interrupted at around 15 km by the east facing scarp and incised topography related to uplift of a topographic bulge. The reduced incision and concave form of the pediment for a few km upslope of the anticline suggests sediment deposition in this zone. The swath profile **C-C'** traces the approximate crest of the topographic bulge, showing changes in relief along the length of the scarp and an overall reduction in elevation in a north-west, downslope, direction.

Figure 3, A to E illustrate the topographic bulge and channels studied, with the location and extent of the images shown in Figure 2A. **3A-** is a hillshade draped over a 2m resolution DEM derived from a pair of 1.5m SPOT-6 images and viewed in 3D with a 5-fold vertical exaggeration. The view is looking

approximately towards the southwest. The paths of the northern, central and southern channels discussed in the text are given, as is the location of the eastern scarp of the topographic bulge that has blocked the northern and central channels and the western scarp of this elevated topographic feature further downstream. Offset linear sections of the eastern scarp are indicated by the dashed pink lines. **3B-** shows one of the SPOT-6 images used to derive the DEMs used in the topographic analyses. The location of the surface mining and the claypan discussed in the main text are given. **3C-** shows the locations of monoclonal flexures, digitized from the 1:100 000 scale geological map of Garcia et al. (2013) and overlain on a hillshade. **3D-** illustrates the path of the channel swath profiles for the northern, central and southern channels (red boxes) and the topographic swath profile that traces the base of the eastern scarp (yellow box) in Figure 9. Numbered yellow circles refer to cosmogenic nuclide sample sites described in the main text and Tables 1 and 2. The grey star is the ^3He sample location of Evenstar et al. (2017). **3E-** A surface model of slope gradient shows the path of the paleochannels where they have incised into the topographic bulge and the intervening smooth, flat surfaces, or interfluves. Aside from the mining buildings, the only steep slopes in the area relate to scarps and fluvial incision.

Figure 4A- A panorama shot of the southern channel sampling site (site 3) showing a preserved coarse clastic bar in the center of the channel to the right of the people and steep, incised banks. **4B-** shows the smooth, low relief topography of the crest of the topographic bulge, where interfluve samples were collected for cosmogenic nuclide analysis. The surface is covered by a thick layer of gypsum dust.

Figure 5. An example of a Raman spectrum (sample NTA5D), with a main quartz band at 465 cm^{-1} and an adjacent band at 503 cm^{-1} that could represent silanol or moganite.

Figure 6. Individual pebble ages (Myrs) derived from ^{10}Be and ^{26}Al measurements and LSD production rate scaling are indicated for the different sample locations. Values in black are ages derived from ^{10}Be and values in red are ages derived from ^{26}Al . Uncertainties on individual ages are one standard deviation (see text for details). Saturated samples are indicated along with the number of these measurements (n). In general ages decrease southwards suggesting channel abandonment propagated south.

Figure 7. Two-isotope diagrams plotting the samples from which both ^{26}Al and ^{10}Be were measured. **7A** uses LSD scaling (Lifton et al., 2014). **7B** uses Lm scaling (Balco et al., 2008). Both scaling approaches take high latitude-sea level production factors from Borchers et al. (2016). Error ellipses are one standard deviation and green refers to the interfluvial sites (near the crest of the topographic bulge), yellow to the northern channel, blue to the central channel and red to the southern channel. Samples that experience constant exposure should plot, within uncertainties, within the black outlined envelope (or steady-state erosion 'island') extending from the left. Samples that have experienced sufficiently long periods of burial should plot beneath the island, in the zone of complex exposure. The position of the steady-state erosion island is dependent on the production rates and scaling scheme assumed (see main text for more details). The samples denoted by the green error ellipses plotting to the right of the island tip exceed the saturation value predicted by the production rates used. The red dashed lines show the paths samples would follow if they were shielded from cosmic rays after a period of constant exposure.

Figure 8A. A three-isotope diagram of $^{22}\text{Ne}/^{20}\text{Ne}$ against $^{21}\text{Ne}/^{20}\text{Ne}$ for the samples given in table 1. The black lines show the upper and lower bounds for the air-spallation line. Also shown with the individual samples are measurements of the CRUE standard made at the same time. Uncertainties are one standard deviation. **Figure 8B.** A close up of the region shown by the dashed box in **8A**.

Figure 9. The channel profiles are shown in blue and channel-bank profiles in red for the northern, central and southern channels; based on the 500m wide multidirectional swaths indicated by the red boxes in Figure 3D. The bottom panel shows the maximum and minimum elevations in the 500 m wide topographic swath profile measured along the base of the scarp, indicated by the yellow box in Figure 3D. The locations of the channels along the scarp are shown in the bottom panel. The profiles are described in more detail in the main text.

Figure 10. The channel profiles and channel-bank profiles of each channel shown in Figure 9 are given, along with an estimate of the form the channel would take for the northern and central channels if there had been no uplift (dashed line). Beneath the profile plots of the northern and central channels is an estimate of the uplift rates, based on the differences in elevation between the ‘no-uplift’ profile and the abandoned channel profile divided by the age of abandonment. Plots of fluvial incision along the length of all the channels are estimated based on the differences between the channel bank elevation and the elevation of the abandoned channel, divided by the length of time between the end of El Diablo Formation deposition (11 Myr, see main text) and the age of the channel.

Figure 11. The perimeter of Pampa de Tana shows instances of beheading (white arrows) and drainage capture (orange arrow), indicative of the consumption of the interfluvium between the Quebrada de Camarones and Quebrada de Camiña. **A** and **B** refer to the location of the images on Figure 2. The images are from GoogleEarth.

Tables

Table 1. Input used in online calculator age estimates^a

| Sample site ^b | Lat. | Long. | Elev. | Sample ID | Average sample thickness | ¹⁰ Be conc. | ¹⁰ Be conc. 1 s.d. | Be AMS standard flag ^c | ²⁶ Al conc. | ²⁶ Al conc. 1 s.d. | ²¹ Ne conc. | ²¹ Ne conc. 1 s.d. | Ave. ²¹ Ne conc. ^e | Ave. ²¹ Ne conc. 1 s.d. |
|--------------------------|-----------|-----------|----------|-----------------------|--------------------------|------------------------|-------------------------------|-----------------------------------|------------------------|-------------------------------|------------------------|-------------------------------|--|------------------------------------|
| | Dec. Deg. | | m.a.s.l. | | cm | x10 ⁶ at/g | | | x10 ⁶ at/g | | | | | |
| 1 | -19.35292 | -69.87942 | 1291 | TA1A | 1.5 | 20.6 | 0.6 | NIST_30600 | | | 276 | 11 | | |
| | | | | TA1B | 1.5 | 22.3 | 0.6 | NIST_30600 | | | 188 | 12 | | |
| | | | | NTA-1D | 1.0 | 17.4 | 0.6 | 07KNSTD | | | 56.5 74.2 84.4 | 6.9 12.5 7.0 | 77.7 | 14.1 |
| | | | | TA06-1G | 2.0 | 15.7 | 0.6 | 07KNSTD | | | 49.6 | 11.9 | | |
| | | | | TA-1K | 2 | 15.1 | 0.5 | 07KNSTD | 58.5 | 2.8 | | | | |
| 2 | -19.39231 | -69.83283 | 1323 | TA2B | 3.0 | 11.3 | 0.4 | NIST_30600 | | | 37.4 | 7.3 | | |
| | | | | NTA2D | 1.5 | 15.5 | 0.5 | 07KNSTD | | | 85.4 | 21.7 | | |
| | | | | NTA2F | 1.0 | 17.8 | 0.6 | 07KNSTD | | | 33.3 92.4 | 19.4 22.8 | 62.8 | 41.8 |
| | | | | TA2M | 3.0 | 13.8 | 0.5 | 07KNSTD | 62.6 | 3.9 | | | | |
| | | | | TA2N | 0.5 | 12.7 | 0.5 | 07KNSTD | | | | | | |
| | | | | TA2P | 4.0 | 14.6 | 0.5 | 07KNSTD | | | | | | |
| 3 | -19.40353 | -69.82064 | 1312 | TA3B | 1.0 | 1.7 | 0.1 | NIST_30600 | | | 13.6 9.8 | 6.1 4.0 | 11.7 | 2.7 |
| | | | | TA06-3F | 1.0 | 8.68 | 0.31 | 07KNSTD | 36.5 | 2.3 | | | | |
| | | | | TA-3M | 2.5 | 0.698 | 0.054 | 07KNSTD | | | | | | |
| | | | | TA-3N | 2.0 | 0.777 | 0.047 | 07KNSTD | | | | | | |
| | | | | TA-3P | 1.5 | 3.63 | 0.20 | 07KNSTD | | | | | | |
| 4 | -19.40444 | -69.82083 | 1315 | TA4C | 2.0 | 19.4 | 0.4 | NIST_30600 | | | 79.4 | 32.8 | | |
| | | | | NTA4D | 1.0 | 16.3 | 0.6 | 07KNSTD | | | 263 291 | 12 16 | 277 | 20 |
| 5 | -19.38647 | -69.83897 | 1337 | TA5A | 2.0 | 24.6 | 0.5 | NIST_30600 | | | 88.4 98.2 | 7.1 17.6 | 93.3 | 6.9 |
| | | | | TA5C | 2.0 | 19.1 | 0.5 | NIST_30600 | | | | | | |
| | | | | NTA5D | 1.5 | 19.7 | 0.6 | 07KNSTD | | | 186 178 149 | 10 9 14 | 171 | 20 |
| | | | | TA-5K | 1.5 | 18.9 | 0.6 | 07KNSTD | 63.2 | 4.1 | | | | |
| | | | | TA-5L | 2.0 | 18.0 | 0.6 | 07KNSTD | 63.7 | 5.4 | | | | |
| | | | | TA06X5a | 1.0 | 19.2 | 0.6 | 07KNSTD | 52.5 | 4.5 | | | | |
| | | | | TA06X5b | 1.0 | 19.5 | 0.6 | 07KNSTD | 60.4 | 3.1 | | | | |
| | | | | TA06X5c | 0.5 | 19.5 | 0.6 | 07KNSTD | 55.9 | 3.5 | | | | |
| | | | | TA06X5d | 1.0 | 16.0 | 0.6 | 07KNSTD | 57.0 | 3.2 | | | | |
| 6 | -19.45399 | -69.94735 | 992 | PIS12-05 ^d | 0.05 | 0.399 | 0.026 | 07KNSTD | 2.48 | 0.19 | | | | |

^a Other input into the online calculator that was consistent for all the samples included: applying the 'std' flag for the atmospheric pressure model; a density of 2.6g/cm³; and a zero erosion rate (see also footnote ^d in Table 2). In all cases topographic shielding is negligible.

^b See Figure 3D for location of samples sites.

^c For consistency between the data measured by two different AMS, some of which was derived prior to the changes proposed to the ¹⁰Be half-life (Nishiizumi et al., 2007; Chmeleff et al., 2010; Korschinek et al., 2010), the online calculator Be isotope standardization 'NIST_30600' was applied to the SUERC data and 07KNSTD to the CologneAMS data. Al data used the KNSTD flag.

^d The sample from site 6 is considered in relation to possible inheritance and no age is calculated.

^e Where multiple assays were measured the arithmetic mean and standard deviation ²¹Ne concentrations are used (Table 2).

Table 2. Cosmogenic nuclide exposure ages

| Sample site location ^a | Site type | Sample ID | ¹⁰ Be derived age ± 1 s.d. ^{c, d} (Myr) | ²⁶ Al derived age ± 1 s.d. ^{c, d} (Myr) | ²¹ Ne derived age ± 1 s.d. ^{c, d} (Myr) |
|-----------------------------------|------------------|----------------------|---|---|---|
| 1 | Northern channel | TA1A | <i>saturated</i> | – | 8.34 ± 0.73 |
| | | TA1B | <i>saturated</i> | – | 5.63 ± 0.57 |
| | | NTA-1D ^b | <i>saturated</i> | – | 2.44 ± 0.28 |
| | | TA-1K | <i>saturated</i> | <i>saturated</i> | – |
| | | TA06-1G ^b | <i>saturated</i> | – | 1.44 ± 0.36 |
| 2 | Centre channel | TA2B | 1.96 ± 0.22 | – | 1.10 ± 0.23 |
| | | NTA2D ^b | <i>saturated</i> | – | 2.41 ± 0.64 |
| | | NTA2F ^b | <i>saturated</i> | – | 1.77 ± 1.19 |
| | | TA2M | 3.77 ± 0.76 | <i>saturated</i> | – |
| | | TA2N | 2.87 ± 0.45 | – | – |
| | | TA2P | 4.76 ± 0.67 | – | – |
| 3 | Southern channel | TA3B | 0.21 ± 0.02 | – | 0.36 ± 0.08 |
| | | TA06-3F | 1.49 ± 0.15 | 1.07 ± 0.20 | – |
| | | TA-3M | 0.10 ± 0.01 | – | – |
| | | TA-3N | 0.11 ± 0.09 | – | – |
| | | TA-3P | 0.54 ± 0.05 | – | – |
| 4 | Interfluvial | NTA4D ^b | <i>saturated</i> | – | 8.18 ± 0.88 |
| | | TA4C | <i>saturated</i> | – | 2.26 ± 0.95 |
| 5 | Interfluvial | TA5A | <i>saturated</i> | – | 2.63 ± 0.29 |
| | | TA5C | <i>saturated</i> | – | – |
| | | NTA5D ^b | <i>saturated</i> | – | 4.93 ± 0.69 |
| | | TA-5K | <i>saturated</i> | <i>saturated</i> | – |
| | | TA-5L | <i>saturated</i> | <i>saturated</i> | – |
| | | TA06X5a | <i>saturated</i> | 2.25 ± 1.01 | – |
| | | TA06X5b | <i>saturated</i> | <i>saturated</i> | – |
| | | TA06X5c | <i>saturated</i> | <i>saturated</i> | – |
| | | TA06X5d | <i>saturated</i> | <i>saturated</i> | – |

^a See Figure 3D for location of samples sites.^b Sample measured by Raman spectrometry. See main text for details.^c One standard deviation uncertainties in the exposure ages are the 'external' uncertainties reported by the online calculator, which take into account analytical as well as estimated production rate uncertainties.^d The ages presented assume zero erosion. This is justified based on many of the samples retaining fluvially rounded forms. If assume a maximum erosion rate of 10 cm/Myr, using the estimates of Nishiizumi et al. (2005), the only significant effect would be that our site 2 ¹⁰Be ages increase. In this case the youngest age (sample TA2B) becomes 2.74 ± 0.52 Myr and samples TA2M, TA2N and TA2P are saturated. As sample TA2B shows evidence for fluvial rounding we assume the assumption of zero erosion is valid, but note our ages should be considered as minimum ages.

Figure 1

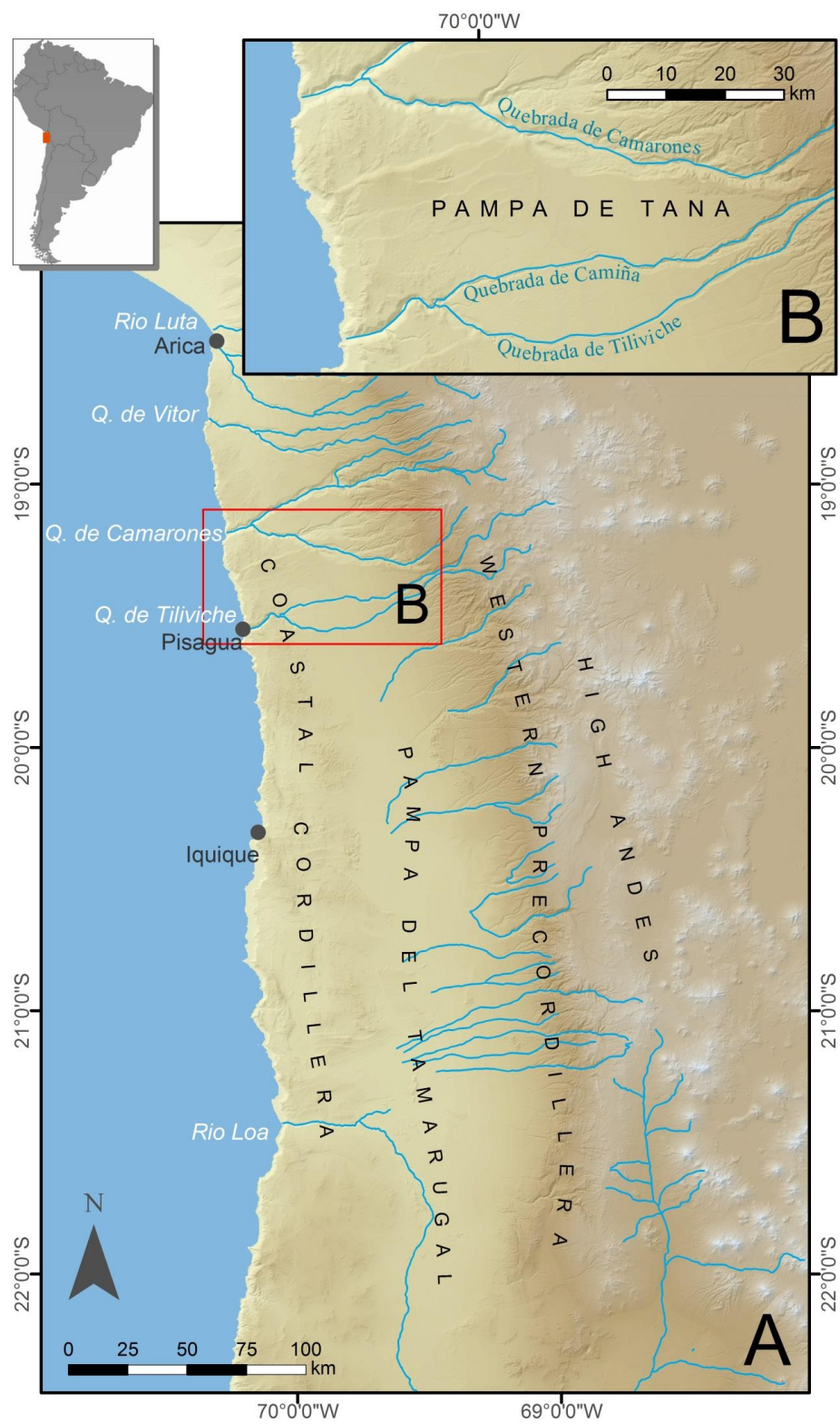


Figure 2

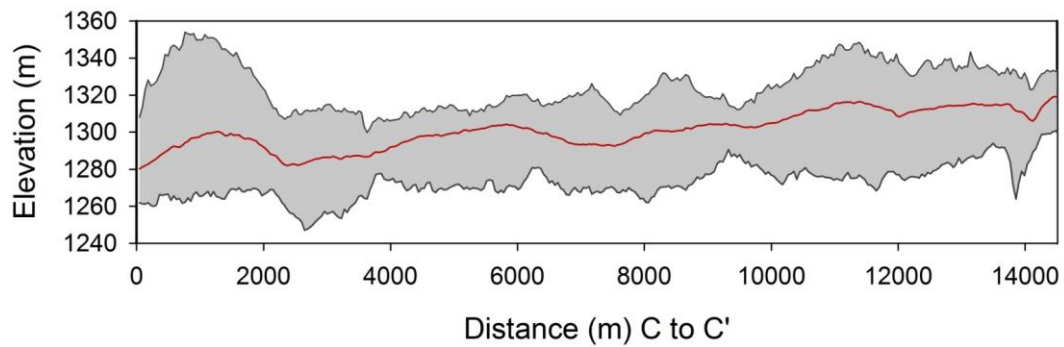
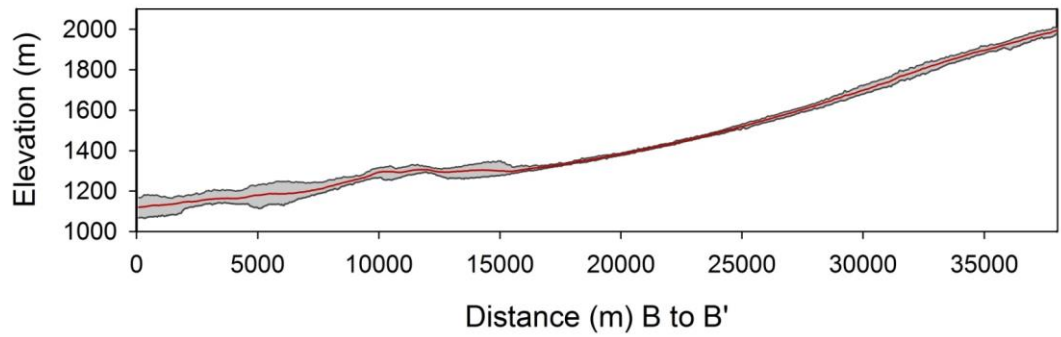
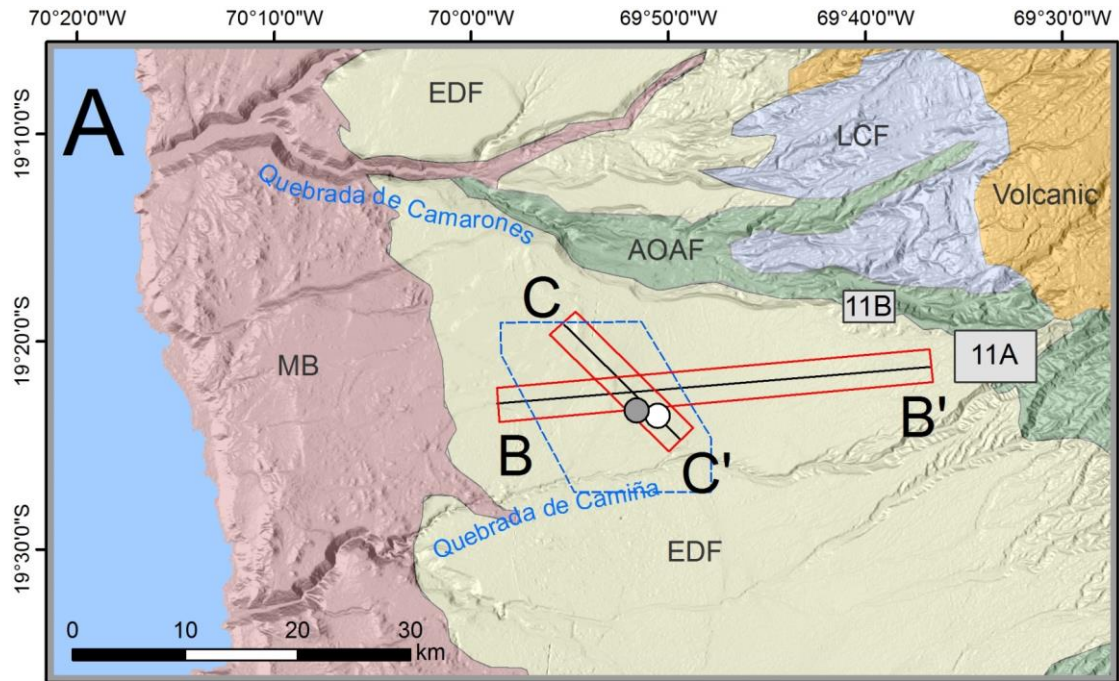


Figure 3

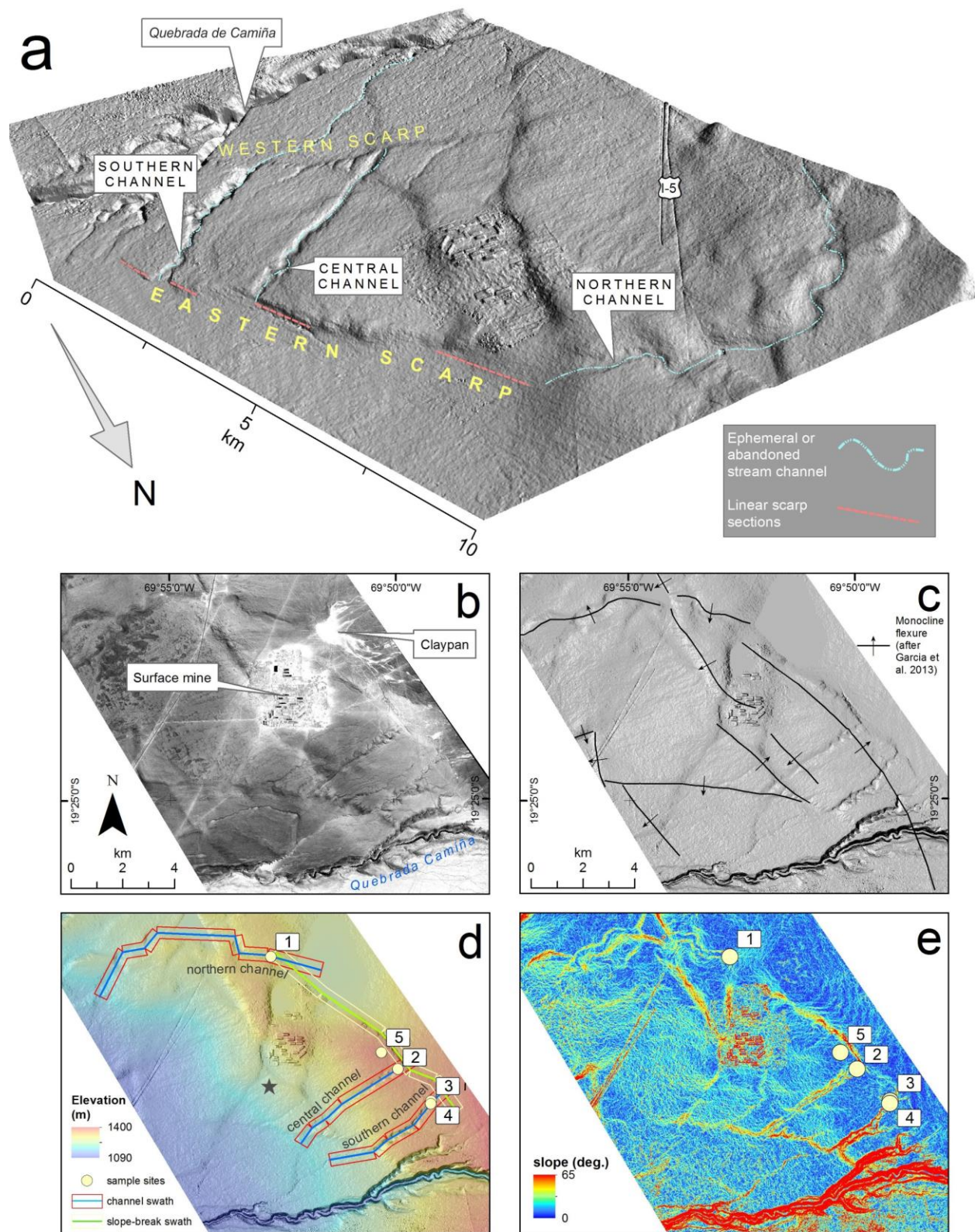


Figure 4

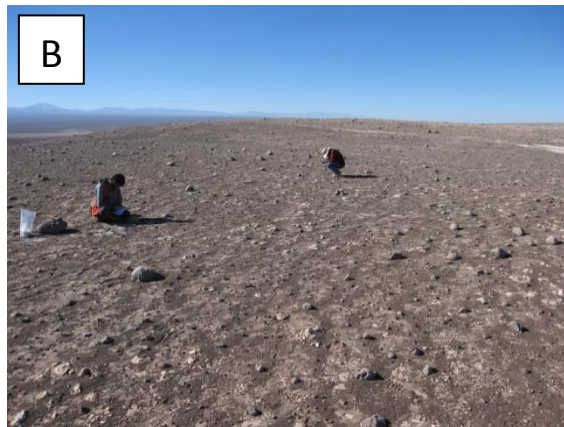
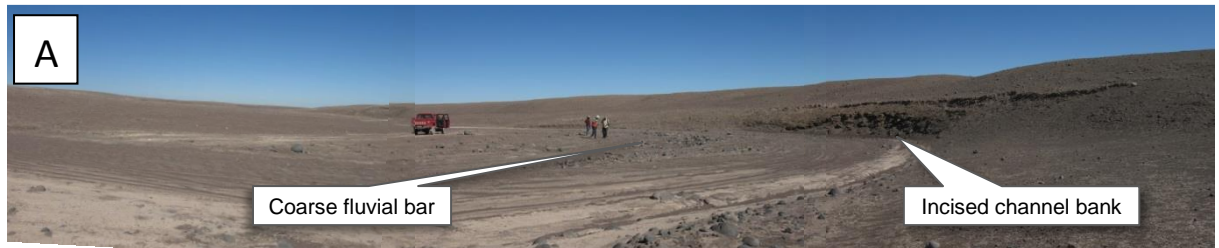


Figure 5

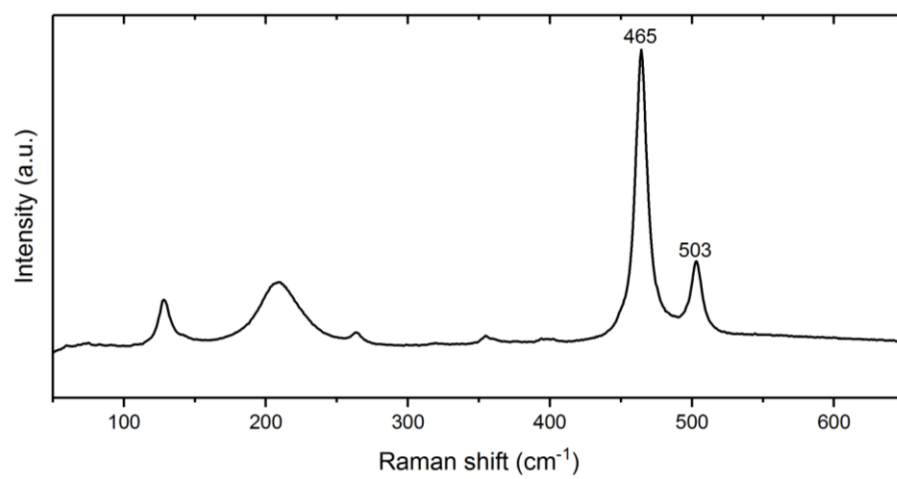


Figure 6

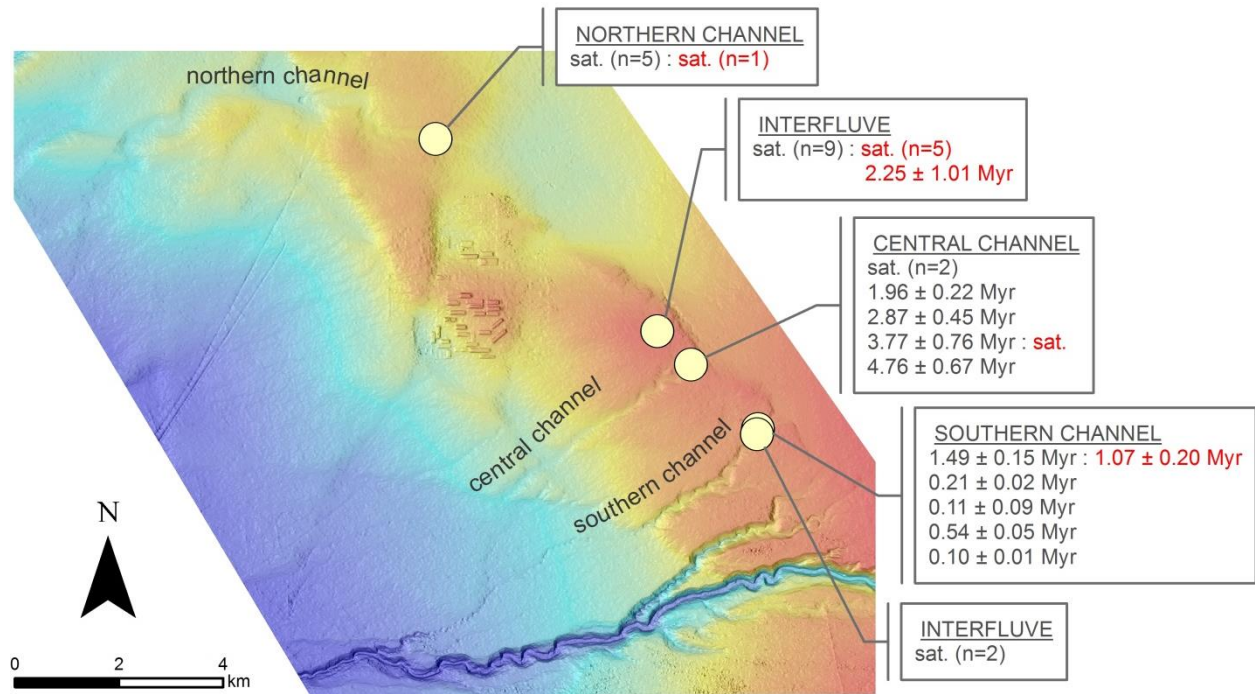


Figure 7

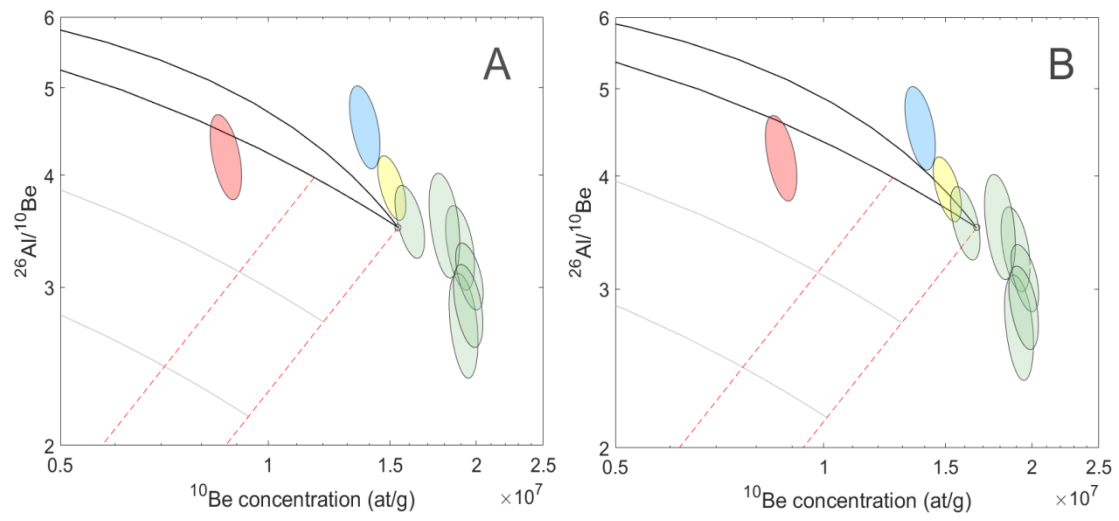


Figure 8

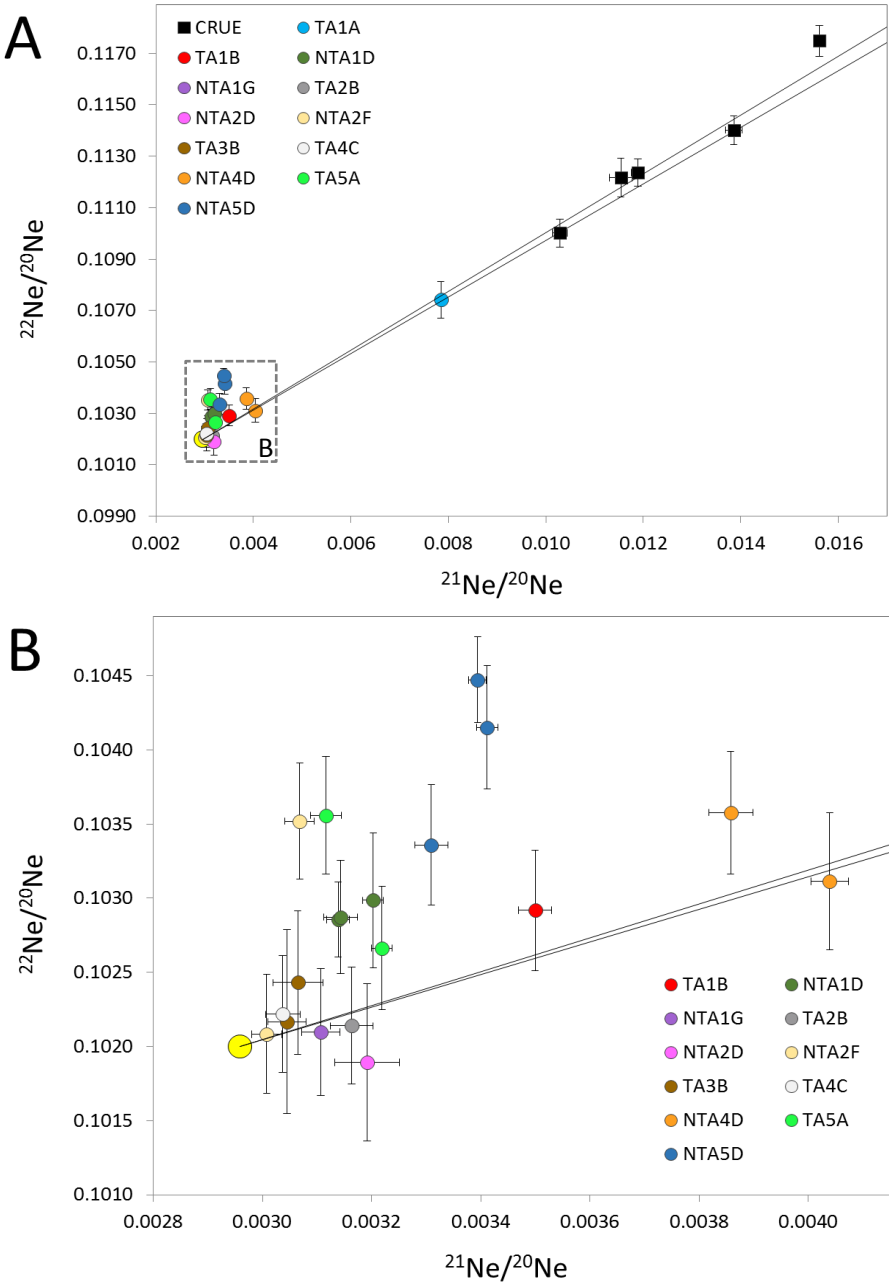


Figure 9

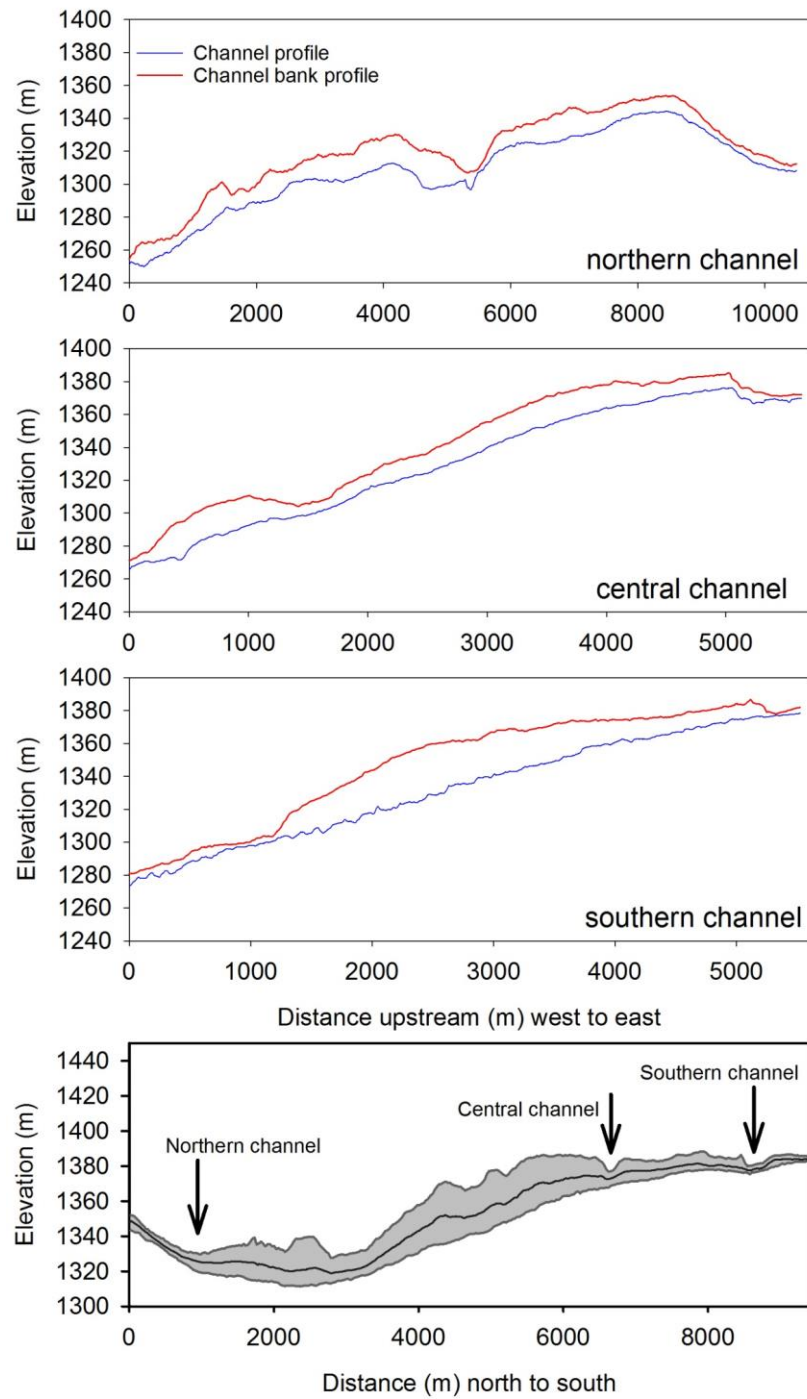


Figure 10

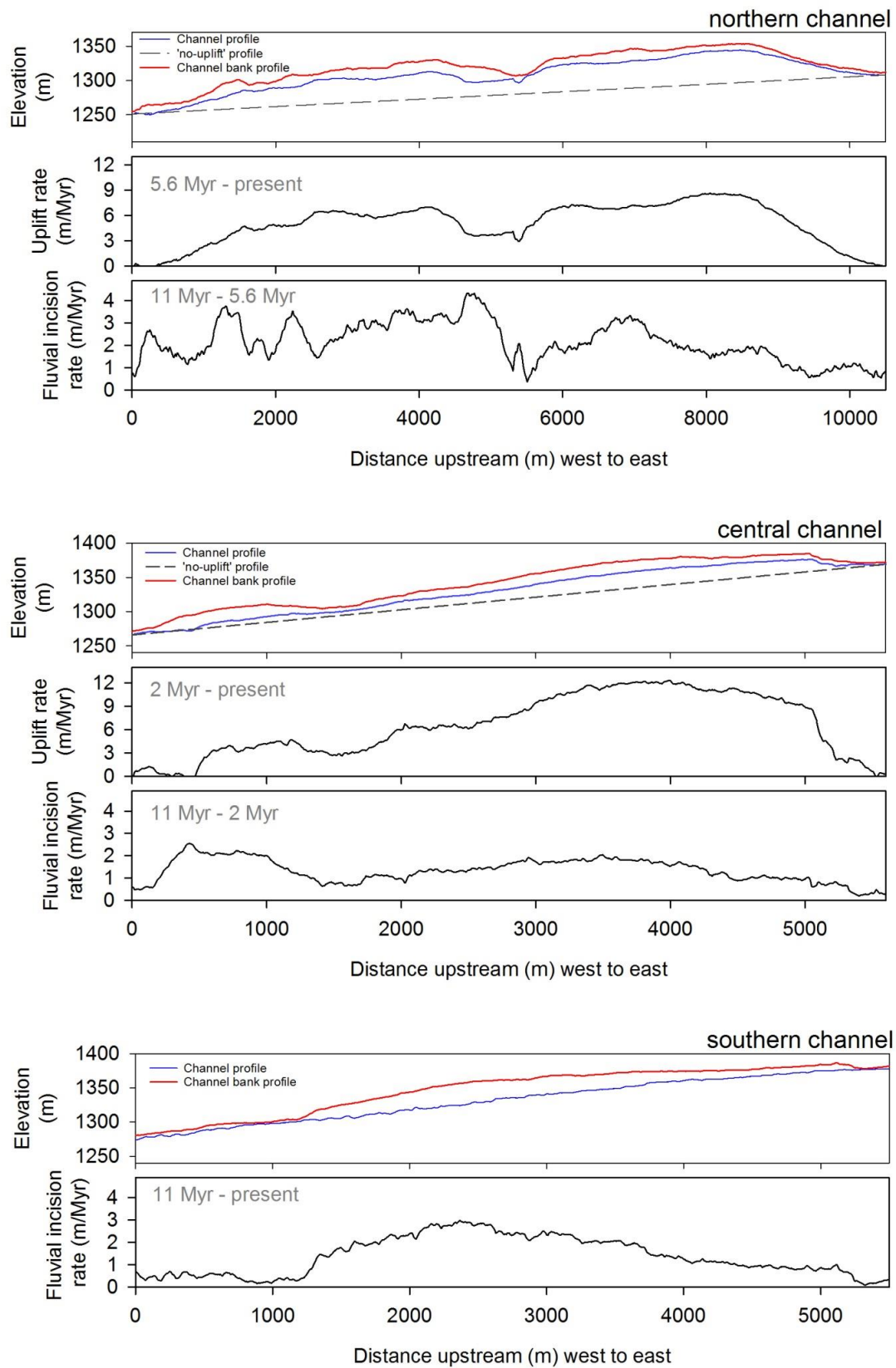


Figure 11

